University of Windsor

Scholarship at UWindsor

2023

Superhydrophobic and Oleophobic Surfaces. Synthesis and Applications

Zirui Liu
University of Windsor

Superhydrophobic and Oleophobic Surfaces. Synthesis and Applications.

By

Zirui Liu

A Thesis
Submitted to the Faculty of Graduate Studies
through the Department of Mechanical, Automotive & Materials Engineering
in Partial Fulfillment of the Requirements for
the Degree of Master of Applied Science
at the University of Windsor

Windsor, Ontario, Canada

Superhydrophobic and Oleophobic Surfaces. Synthesis and Applications.

By

Zirui Liu

APPROVED BY:

_____
J. Ahamed
Department of Mechanical, Automotive & Materials Engineering

_____
R. Riahi
Department of Mechanical, Automotive & Materials Engineering

_____
V. Stoilov, Advisor
Department of Mechanical, Automotive & Materials Engineering

January 6, 2023

DECLARATION OF ORIGINALITY

I hereby certify that I am the sole author of this thesis and that no part of this thesis has been published or submitted for publication.

I certify that, to the best of my knowledge, my thesis does not infringe upon anyone's copyright nor violate any proprietary rights and that any ideas, techniques, quotations, or any other material from the work of other people included in my thesis, published or otherwise, are fully acknowledged in accordance with the standard referencing practices. Furthermore, to the extent that I have included copyrighted material that surpasses the bounds of fair dealing within the meaning of the Canada Copyright Act, I certify that I have obtained a written permission from the copyright owner(s) to include such material(s) in my thesis and have included copies of such copyright clearances to my appendix.

I declare that this is a true copy of my thesis, including any final revisions, as approved by my thesis committee and the Graduate Studies office, and that this thesis has not been submitted for a higher degree to any other University or Institution.

ABSTRACT

Surface patterning is an overwhelming approach to mechanically modifying metal surfaces and improving their tribological properties, such as repellency, lower friction, and more excellent corrosion resistance. Patterned surfaces can be applied to various industrial uses, such as cutting tools, submarines, and self-cleaning surfaces. In this paper, the novel nature-inspired flat-top-pillar "double-undercut" designs were proposed to achieve an apparent angle that satisfies super-hydrophobicity and endure higher pressure on which external forces are exerted. The main objective is to enlarge the change in Gibbs free energy for the system to exhibit a heterogeneous wetting to a homogeneous one by excavation on the surface needed to be patterned to obtain an additional 30% of the atmospheric pressure while maintaining an apparent contact angle of greater than 150°.

The analytical approach yielded decent results showing an extra pressure of more than 3 atm averaged from three different scales of two distinct double-undercut designs calculated by the stability equation derived by the Gibbs free energy. Numerical, finite element analysis was also performed in COMSOL-Multiphysics and demonstrated a Canthotaxis wetting transition phenomenon. An average of 800 pascals of additional pressure was achieved for designs of three distinct permutations of double-undercut angles (50°-40°, 50°-36°, and 40°-36°). Specimens were fabricated on silicon wafers by PolyMUMPs method for proof-of-concept and were ready for the future experiment on apparent contact angle and cross-sectional SEM at post breaching the Cassie-Baxter state.

DEDICATION

I dedicate my dissertation work to my parents, Yunyun Liu and Aijun Yang. Thanks for respecting my decision of studying what I am fond of and providing me with endless support mentally and financially.

Also, I would like to credit my girlfriend Jennifer Li for her company and encouragement.

My best buddies, Jeremy Yin and Downey Yang, have always been there for me whenever it was during our school time or after we separated from school.

Furthermore, I would like to thank the whole Windsor Community for letting me finish my undergraduate and graduate study and enjoy my life safely and happily here for the past 8 years.

ACKNOWLEDGEMENTS

TABLE OF CONTENTS

LIST OF TABLES

LIST OF FIGURES

CHAPTER 1 INTRODUCTION

The interfacial properties of the interaction among solid, liquid, and gas(air) are significant for designing and refining various types of metal workpieces for industrial applications. Hydrophobicity is one of the most common surface properties related to corrosion resistance, enhancing durability, and applicable scenarios for metal workpieces. Super-hydrophobicity can provide even better water repellency with an apparent contact angle greater than 150° for water. Research has proven that hydrophobic/superhydrophobic surfaces achieved solely by chemical or combined chemical and mechanical modifications show decent results in non-wettability and abrasive conditions among metal substrates and liquids. However, mechanical approaches to creating such surfaces are yet to be investigated. In addition, this study adopted the performance parameter, the critical pressure of a designed system that can withstand to maintain its hydrophobicity, for practicality. Furthermore, such surfaces may be implemented on cutting tools in machining for less demand on lubricating liquids and enhanced corrosion resistance, submarines for drag reduction, and self-cleaning materials.

There are some typical examples of hydrophobic surfaces on plants and animals in nature. The well-known lotus leaves effect perfectly demonstrates hydrophobicity as the water droplet remains a sphere shape and can easily roll off the surface. Another instance would be the microstructures on shark's skin, which its tooth-like form can help reduce drag underwater.

Some previous studies on mechanical modifications mostly combined with chemical coatings show that the change in surface energy can be achieved along with lowered surface energy. However, there are no such actual applications due to the lack of

sturdiness when countering external forces, pressures, and contamination while remaining hydrophobic and the complexity and time cost for fabrication. With all these concerns, a novel hierarchical design inspired by natural plants (lotus leaf) was proposed and verified in this study in the order of analytical, numerical, and experimental approaches.

The achievements of this study are the comparisons in critical pressures between the single-stage flat-top-pillar and the double-stage flat-top-pillar designs for three sets of different undercut angles with the same structure-to-structure spacing and dimension in height. The analytical approach provides rough predictions on the critical pressures deriving from surface energy. The numerical analysis of the critical pressures conducted in COMSOL-Multiphysics 5.6 with the detailed setup and configurations will be presented later in chapter 4.

Two distinctive types of modifications will be able to vary the surface roughness of material mechanically. One is the protrusion, namely adding an element on top of the substrate, and the other is depression meaning extracting the element from the substrate. Fabrication-wise, the former type was selected to create samples of the proposed design. PolyMUMPs, a three-layer polysilicon surface micromachining process, possibly meet almost every criterion needed for proof-of-concept after reviewing the existing state of the art. A total of nine designs in three different shapes and undercut angles were prepared using "MEMS L-edit" for fabrication and testing. Details on the fabrication of samples will be discussed later in the experiment's setup. Every sample prepared in PolyMUMPs will be placed under the goniometer in a pressurized chamber to simulate external pressures and observe the apparent contact angles of the water droplet.

1.1 Thesis Outline

Chapter 2 is the introduction to hydrophobicity/super-hydrophobicity, along with relative equations and formulae. The definitions of wetting and non-wetting regimes are discussed. Moreover, the previous studies on lowering surface energy and converting surfaces to be more hydrophobic with corresponding apparent contact angles are presented. Modern technologies of creating asperities on metal surfaces will be included. Also, the main objectives and goals are addressed.

Chapter 3 contains the analytical approach to the issued problems. Elaboration on obtaining the formula of critical pressure, particularly for the flat-top-pillar type of asperity, is included in this section. Results and discussion regarding each set of designs are given as well.

Chapter 4 states the numerical method for simulating each design. Restrictions and limits were applied to have every design under the same condition as possible. Therefore, the obtained critical pressures are compared reasonably. Results and discussion are also included.

Chapter 5 illustrates the design parameters, restrictions, and processes in L-edit.

CHAPTER 2 LITERATURE REVIEW

2.1 Hydrophobicity/Super-hydrophobicity and wetting

A well-known example that can elaborate hydrophobic phenomenon is the lotus leaf effect. As the raindrop or condensed water droplet gathers together, showing an almost perfect sphere shape, it would most likely roll off the lotus leaf with a slight tilt angle (Figure 1) [W. Thielick, 2007].
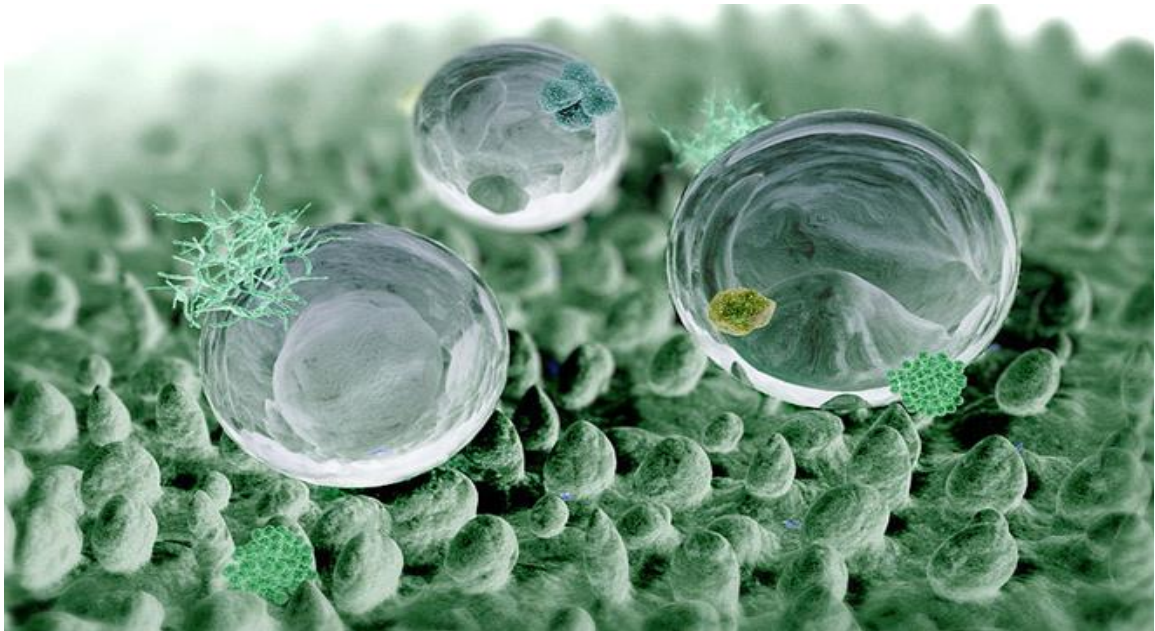
FIGURE 1. LOTUS LEAF EFFECT (W. THIELICK, 2007)

Over 200 different plant surfaces (hydrophobic) had been investigated on their roughness [1], which has a significant impact on hydrophobicity. Lotus leaf maintains excellent super-hydrophobicity owing to its hierarchical structure, namely microscale protrusions covering with nanoscale hair-like structures shown in Figure 2 (a and b).
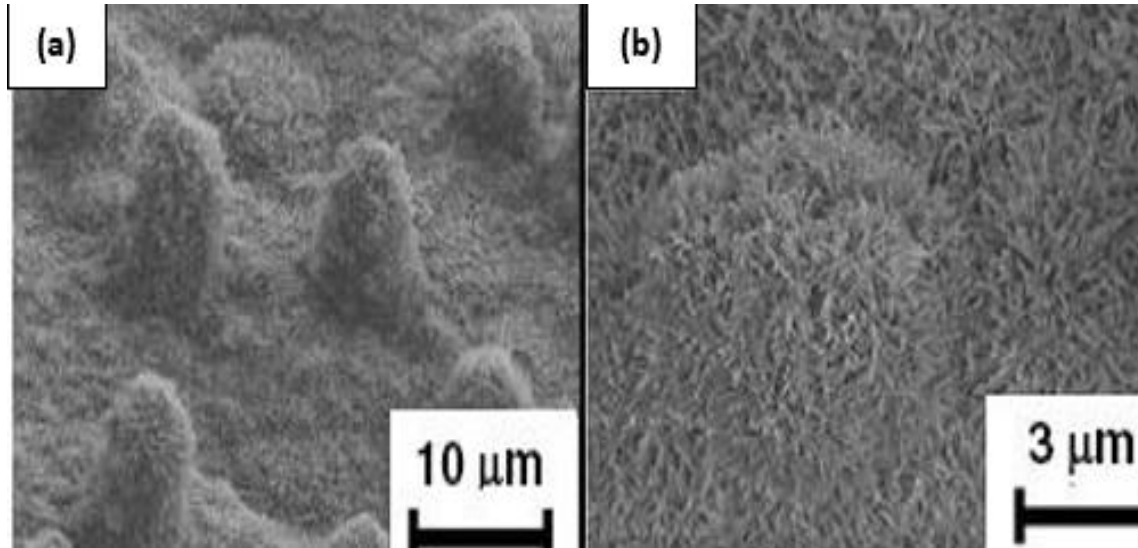
FIGURE 2. SEM OF (A) MICRO-SCALE PAPILLAE ON LOTUS LEAF, AND (B) NANO-SCALE HAIR-LIKE STRUCTURE ON THE PAPILLAE

Such surfaces could also be found in many insects, such as water strider's legs full of micro-setae with fine nano-grooves [2]. The determined water contact angle of the water strider's leg is 167°, meaning super-hydrophobicity could help repel water for its survival on water. Lotus leaf exhibits the most stable superhydrophobic performance overwhelming among the 200 plants, as mentioned earlier, due to its unique hierarchical (multi-scales) structure and the chemical composition of its epicuticular wax on the surface.

Another interesting surface structure that existed on the sharkskin was reported by Bechert et al., showing full of tooth-like riblets with corrugated grooves in Figure 3. These longitudinally arranged grooves achieve a reduction in the formation of vortices. Thus, drag reduction is significantly enhanced [3].
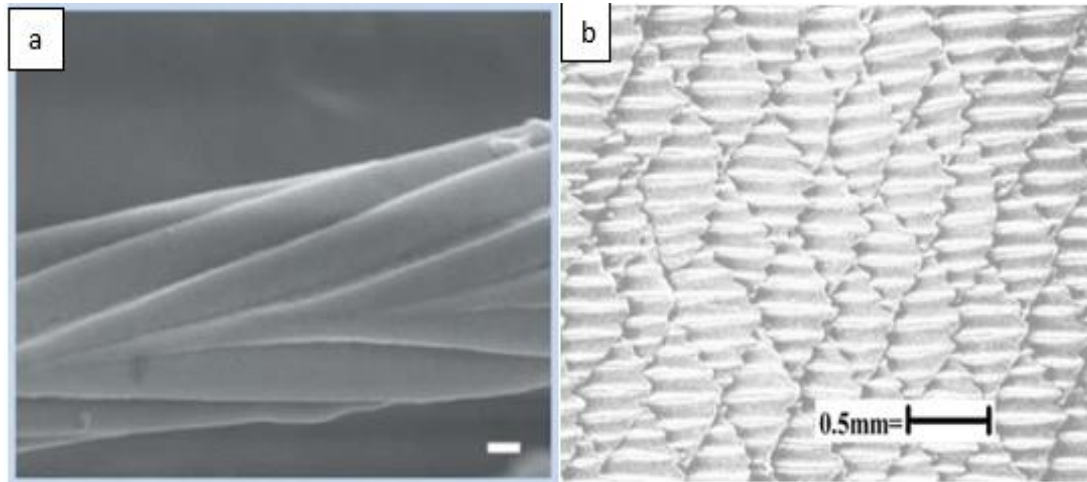
FIGURE 3. SCANNING ELECTRON MICROSCOPE OF (A) THE NANOSCALE STRUCTURES WITH GROOVES OF WATER STRIDER'S LEG (SCALE BAR: 200NM); (B) RIBLETS WITH CORRUGATED GROOVES

This nature-inspired structure and hydrophobic phenomena have consequently triggered numerous studies and investigations on the all-around aspects of hydrophobicity for science or industrial purposes.

Wetting scenarios can be illustrated and categorized by the contact angle with water on any surface to relate the wetting phenomenon to hydrophobicity. Fist two are called Super-hydrophilic and hydrophilic regions, which the contact angles range from 0° to 10° and 10° to 90°, respectively. The last two, which this study is mainly concerned about, are hydrophobic and Superhydrophobic, in which the contact angles range from 90° to 150° and above 150°. One more specific characteristic of Superhydrophobic surfaces is low contact angle hysteresis (difference in angles between receding and advancing side of the water droplet), usually less than 10°. With low contact angle hysteresis, only small sliding angles are required for Superhydrophobic surfaces to have the water droplet rolling down from themselves. In addition, the incorporation of both the adhesive force of any dust

particles or containment to the surface and the capillary force exerted at the liquid-gas interface contribute to the self-cleaning effect.

Several theoretical models have already been constructed over the years to comprehend wetting regimes. First off, it is well recognized that Young's equation (Eq.1) illustrates the relationship between the intrinsic contact angle θ and surface tensions γ for a water (liquid) droplet resting on a flat and smooth surface (Figure 4).

$$cos\theta = \frac{\gamma_{sv} - \gamma_{ls}}{\gamma_{lv}}$$ Eq. 1

Where γ_{sv}, γ_{ls}, and γ_{lv} correspond to interfacial energy per unit area of the solid-vapor, liquid-solid, and liquid-vapor. Nonetheless, this model only describes the properties mentioned above on a smooth surface. Wenzel's model introduced the surface roughness r to Young's equation. Also, the concept of apparent contact angle $cos\theta_w^*$ was brought to Wenzel's model, in which the system undergoes on a rough surface[4]. As shown in Figure 5a, the system is experiencing a homogeneous wetting, where the entire area under the droplet is in contact with the solid surface.
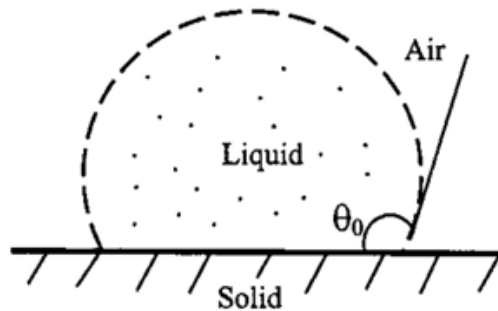
FIGURE 4. DROPLET RESTING ON A SMOOTH SURFACE [BHUSHAN AND JUNG, 2008]
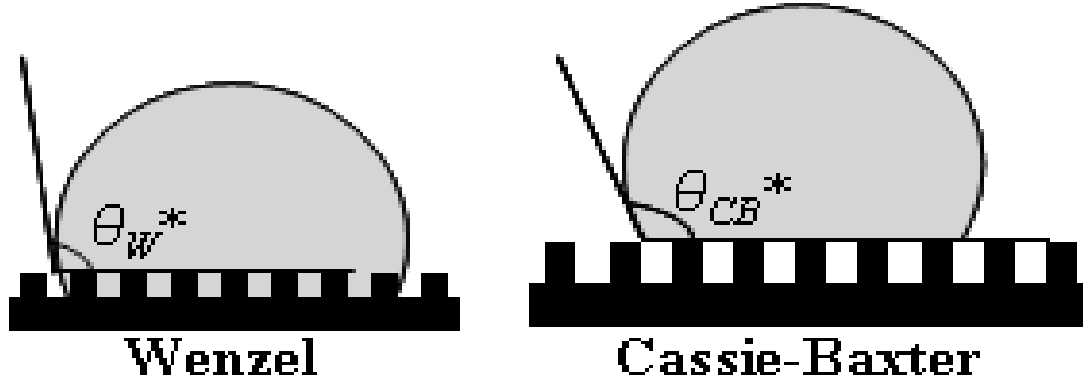
FIGURE 5. (A) WENZEL'S MODEL, A STABLE HOMOGENOUS WETTING SYSTEM; (B) CASSIE-BAXTER'S MODEL, A META-STABLE COMPOSITE WETTING SYSTEM. [CANNON, A., 2008]

Moreover, surface roughness states the ratio of the overall area of a rough surface to the projected area, which should always be greater than 1. According to Eq. 2, this roughness factor can amplify either hydrophobicity of an inherently hydrophobic surface or hydrophilicity of a naturally hydrophilic surface.

$$\cos\theta_w^* = r\cos\theta \qquad\qquad \text{Eq. 2}$$

Later, modification to Wenzel's model was introduced by Cassie and Baxter (Figure 5b), addressing the wetting condition of the heterogeneous surface consisting of two separate materials, resulting in a different contact angle $\cos\theta_{CB}^*$. As shown in Eq.3, f_1 and f_2 are the area fractions, while θ_1 and θ_2 are the corresponding contact angles [5].

$$\cos\theta_{CB}^* = f_1\cos\theta_1 + f_2\cos\theta_2 \qquad\qquad \text{Eq. 3}$$

However, Eq.3 can be rewritten as Eq. 4 when f_2 is the area fraction of air trapped under the water droplet. Since air is hydrophobic, $cos\theta_2 = cos180° = -1$ eliminates $cos\theta_2$. And the contact area fraction turned to be solely φ (liquid-solid) instead of the aforementioned area fractions f_1 and f_2 because of rewriting f_2 as $1 - f_1$.

$$cos\theta_{CB}^* = \varphi(cos\theta + 1) - 1 \qquad\qquad Eq. 4$$

Neither the Wenzel equation nor the Cassie-Baxter equation could provide a most stable contact angle related to the absolute minimum of the Gibbs free energy curve, even though both offer a decent estimation [6]. In addition, naturally hydrophilic surfaces ($\theta <$ 90°) are able to be transformed hydrophobic with proper modifications. And specific requirements on the relationship of liquid-air are fraction and roughness factor for hydrophilic surfaces were provided by Jung and Bhushan (2006) for the transformation [7].

2.2 Approaches to achieving hydrophobicity (State of the Art)

Numerous methods have been developed to modify surfaces to be hydrophobic. These methods can be categorized into two types: chemical and mechanical. Even though they both serve a common goal of reducing the overall surface energy and repelling the liquid phase, the characteristics and constraints are utterly different. In addition, an alternative classification of such asperities on hydrophobic surfaces can be described as protrusion or depression, adding up elements from the bottom or removing elements from plane surfaces. Studies demonstrate different surface patterning created by one of the methods mentioned above with appealing experimental results regarding friction reduction,

large apparent contact angles, etc. However, more considerations need to be taken for practicality and actual industrial applications.

2.2.1 Chemical Method

The coating is one of the most straightforward approaches for hydrophobic modification to metal surfaces, which can be applied to various substrates to lower its surface energy. The chemical composition of coatings primarily controls the surface energy of a substrate. By synthesizing a class of hydrophobic polyhedral oligomeric silsesquioxane (POSS) molecules with the proper mass fraction, Anish et al. have created a superhydrophobic surface on a silicon wafer with the advantage of high surface concentration and surface mobility of $-CF_3$ and $-CF_2$ groups achieving a high receding contact angle of 124.5° with a relatively low contact angle hysteresis of $\pm 1.2°$ [8]. Sungnam et al. demonstrated that the super hydrophobicity on an aluminum substrate was established chemically by applying a heptadecafluoro-1,1,2,2-tetrahydrodecyl trimethoxy silane (HDFS) coating, which the corresponding contact angle with water sits at 160°. For comparison, the same uncoated substrate shows an apparent contact angle with water of 0° [9]. Chemical vapor deposition (CVD) as one of the main approaches for coating has also been widely adopted for hydrophobic modification. In the experimental studies conducted by Miwa et al., with the aforementioned chemical groups ($-CF_3$ and $-CF_2$), a similar chemical surfactant, heptadecafluorodecyltrimethoxysiliane (FAS-17), was applied by such CVD method on Pyrex glass plates, which formed a hydrophobic film regarding the reduction on surface energy. The contact angle with water for a chemically coated flat glass plate was maintained at 105° [10]

Although it is relatively straightforward to reduce surface energy chemically, there are multiple constraints regarding purely chemical passivated films and coatings when external abrasive forces, pressures, and high flow rates are considered. Specifically, the worn-out phenomenon of coatings and films will decrease hydrophobicity's effectiveness and reduce contact angle with water under high flow rate, higher external pressure, and forces. Also, it is suggested that low surface energy provided by chemical passivation was not the only factor that contributed to a system's hydrophobicity. That is due to the surface migration of the chemical solvent during a specific deposition process (CVD), which changed the topography of the surface of the substrates. Thus, it leads to structure-oriented solutions that modify the system's overall liquid-solid contact area and gas fraction.

2.2.2 Mechanical Method

Various approaches have been adopted to create different surface patterns to reduce the liquid-solid contact area, thus increasing the gas fraction of a desired hydrophobic system. Despite the coating deposition of chemical surfactants for surface energy lowering purposes, the change in roughness caused by the electrospinning process of the coating was captured by X-ray photoelectron spectroscopy displaying a surface migration. The significance of the roughened surface during the deposition process is that it can lower the need for POSS concentration, maintaining the system in the Cassie/meta-stable state. Taking into consideration surface texturing, further investigation of this study focused on the topography of the patterned surface on Silicon wafer. Even without any chemicals coated, protrusions with re-entrant curvature, an undercut structure on the etched surface have contributed to a high advancing angle of 143°, compared to a low advancing angle of 10° for a smooth surface. Furthermore, it was deemed that the unique "undercut" structure

has been the main factor of reaching extremely high hydrophobicity [8]. Also, electro spun

fibers significantly enhance hydrophobicity, which even turns an inherently oleophilic

surface into oleophobic. Electrospinning method in general can be applied to deposit nano

or micro-scale patterns onto surfaces in any shapes [11]–[14]. The mechanism behind this

technique is to deposit randomly oriented nonwoven fiber mats, which was caused by the

inherent electrostatic unstableness of the charged jet when it projects from the spinneret to

the collector shown in Figure 6. Significantly, the DC-biased AC-electrospinning offers a

more stabilized control on the microstructures, which enhances the hydrophobicity of the
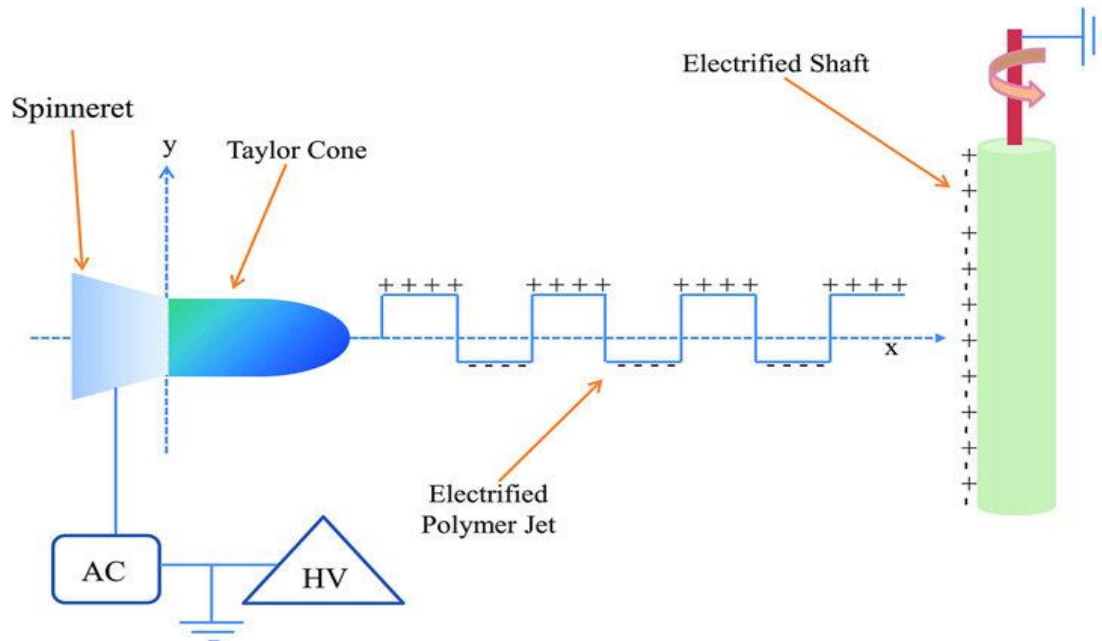
FIGURE 6. SCHEMATIC DIAGRAM FOR AN ELECTRIFIED POLYMER JET DURING DC-BIASED AC-ELECTROSPINNING [F.O. OCHANDA, 2012].

system with the deposited asperities. That leads to the entrapped air between each

microstructure and enlarges the projected gas fraction [15]

Chemical etching by anodization is also adopted for the ease of fabrication to create

random porous textures on metal surfaces. Sungnam Lyu et al. have created randomly

textured aluminum plates by such method. Oxalic acid solution at a constant voltage of 40V and temperature of 26℃ has anodized the aluminum plate for 12 hours, which formed an arbitrarily shaped coral-like anodic oxide film of both micro and nano-scaled structures shown in Figure 7 [9]
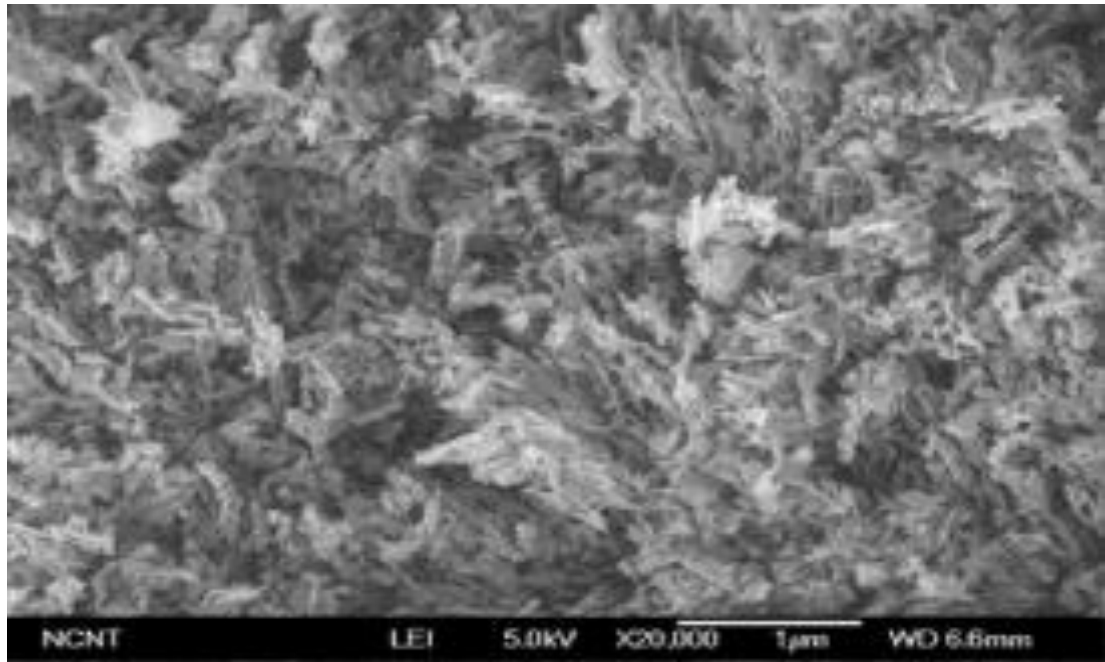
FIGURE 7. MULTI-SCALED CORAL-LIKE STRUCTURES ON THE ANODIZED ALUMINUM PLATE AT **26℃**. [SUNGNAM LYU, 2013]

Similar to anodization, another intriguing approach is calcination. Miwa et al. have generated textured Pyrex glass plates, which were first coated by a mixture of boehmite powder and aluminum acetylacetonate (AACA) with ethanol, then calcinated five times. They were able to control the roughness by varying the boehmite to ethanol ratio, resulting in different sizes of irregularly shaped nanostructures [10]

The methods mentioned above can only generate asperities in random or arbitrary shapes, which is not ideal for discovering the in-depth characteristics of surface patterns

affecting the overall hydrophobic behaviour. However, some approaches can offer regular, manually controllable shapes of textures.

Among the more geometry controllable mechanical methods, lithography is the most commonly adopted one, which can produce organizable arrays of regular shaped patterns on the substrate by etching through the mask (photoresist) through irradiation. There are several variants for lithography, namely, E-beam lithography X-ray lithography and near-field scanning optical lithography, which offer nano-scaled surface patterns [16]–[18]. However, they are not desired for mass production and the low cost-effectiveness. Meanwhile, the photolithography method is capable of mass-producing for squared depression type ($5\mu m$ deep) of patterned substrates but limited to its minimum size due to diffraction limit.

Alternatively, micro-machining has been chosen to modify different types of substrates, where channels and valleys can be produced by sliding the indenter during such a process [19] Laser ablation technique was also found to be effective for most types of substrate materials, for example ceramics, metals, polymers and crystalline structures, as it melts down element so quickly from the substrate leaving minimal damage to the bulk structure [20]. In addition, it provides better control on the shape and size of the patterns without accessory process like photoresist. However, the heat generated during laser texturing causes material melt-down around the edges of the dimples shown in Figure 8 is

inevitable [21] In addition, this type of method cannot establish a multi-scaled geometry of asperities on substrates, or any kind of complex patterns with undercut.
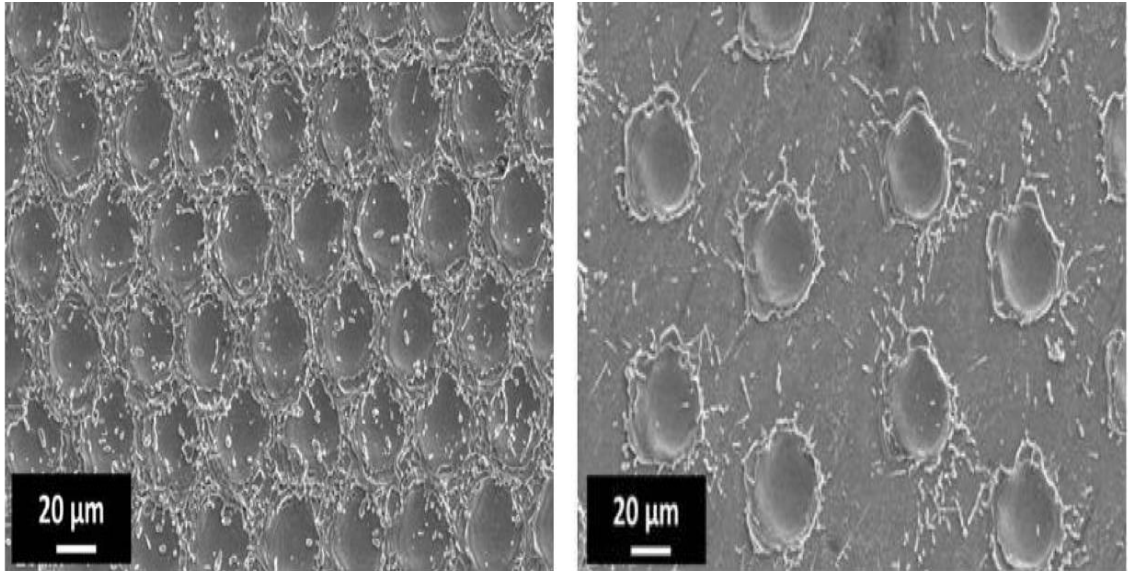
FIGURE 8. SEM DIAGRAMS OF LASER ABLATED SUBSTRATES, SHOWING SPLASHES AROUND THE EDGE OF DIMPLES FOR TWO DIFFERENT ASPECT RATIOS (DISTANCING BETWEEN EACH DIMPLE).

Existing mass production methods include hot-embossing/rolling, injection molding, and curable polymer systems or the hot-embossing approach, the master structure is pressed into the desired substrate heated up to proper temperatures for softness [22], [23]. When the system is cooling down, there is a chance that the substrate may carry on flowing due to the contact with the master structure, which results in a loss of precision. Higher pressures will be needed for embossing for low heat-up temperatures, which may lead to deformation for both the substrate and master. The challenging point for injection molding is large aspect-ration (depth/width), which is not applicable for complicated structures. The long curing time makes it not time-effective for epoxy curable polymer systems to mass-produce, even though it can be applied on a variety of materials.

12

The drastic development of silicon micro/nanochips has been controversial these years. The channelling and the ability to achieve sophisticated topography can be taken advantage of among other available means. Structures with re-entrant curvature, also known as the "undercut," can be established upon this approach[8] This layer-by-layer
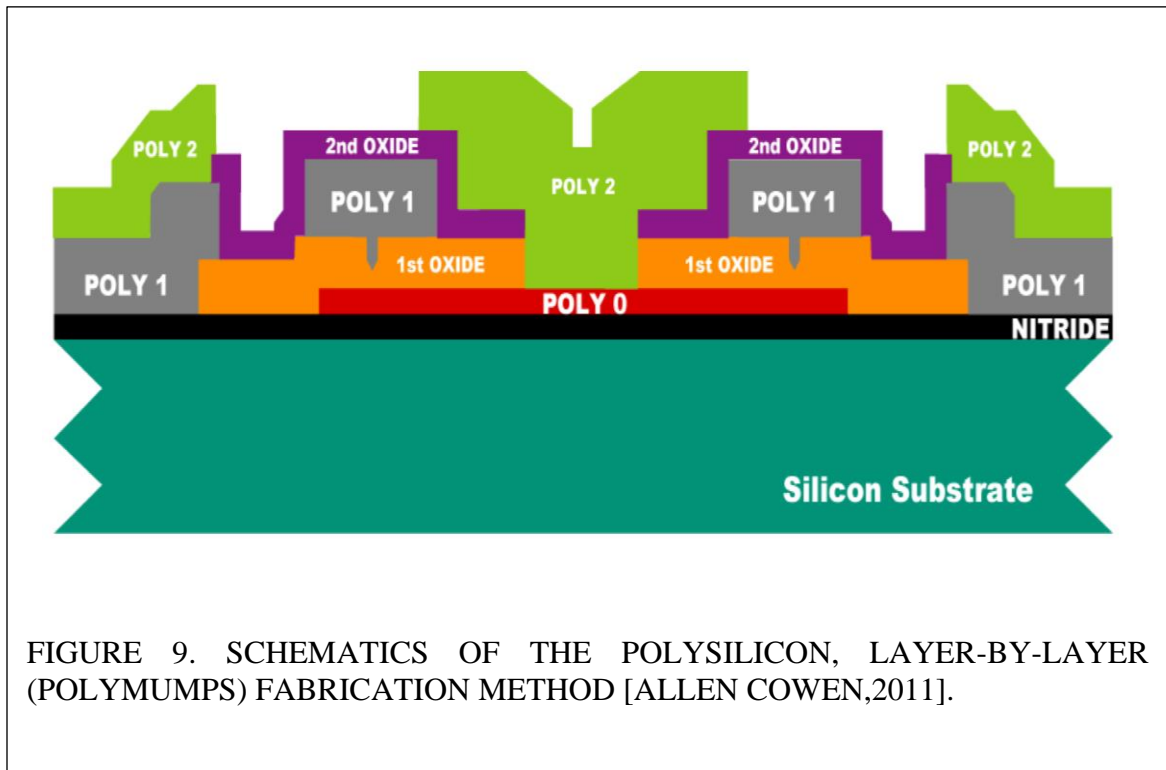
FIGURE 9. SCHEMATICS OF THE POLYSILICON, LAYER-BY-LAYER (POLYMUMPS) FABRICATION METHOD [ALLEN COWEN,2011].

architecture requires polysilicon and deposited oxides as the sacrificial layer to create desired geometries [24].The complexity of geometry of this fabrication method can be demonstrated in Figure 9. Lithography will be utilized for patterning, and the asperities will be planted onto the sacrificial layer (phosphosilicate glass) via the Reactive Ion etching method. The PSG layer is first deposited by the low-pressure chemical vapour deposition method and then annealed for greater hardness. This enhances resistance to etching chemicals to ensure precise pattern transfer into the polysilicon architecture. This fabrication process also presents a plasma etch system for the first silicon layer.

The aforementioned methods of obtaining hydrophobicity by modifying surfaces are addressed along with their pros and cons. Thus, polysilicon shows its advantages in achieving complex geometries while maintaining fabrication precision for later investigation on the mechanical characteristics of hydrophobic surface patterning. Plus, it is desirable for customizing and designing novel patterns and geometries to examine the proof-of-concept. Detailed description regarding the fabrication will present in later Chapters.

2.3 Drag Reduction&Stability (Performance Characteristics)

Studies have both theoretically and numerically verified the drag reduction of superhydrophobic surfaces containing micro-protrusions from different aspects. Also, experiments showing compelling drag reduction on both laminar and turbulent flow were carried out [25]–[31]. The so-called "slip" effect primarily contributes to the reduction in drag, where the air is trapped between the liquid and the solid sides, and the shear stress can be greatly mitigated, correspondingly. Another beneficial point that patterned hydrophobic surfaces could offer is reducing friction due to the decrease in the actual contact area. Similar to drag reduction, the trapped air layer between each asperity behaves in the form of lubrication for abrasive motions [9]. At the same time, the liquid-solid interface produces resistance to the flow due to adhesive wetting of surface energy. Key factors mechanically benefiting the hydrophobicity of surfaces are surface roughness and the multi-scaling (hierarchical) morphology.

Mohamed A. Samaha et al. have modeled a series of numerical simulations regarding drag reduction and stability performance on superhydrophobic surfaces with random roughness compared to homogeneous roughness [15]. The gas fraction meaning

shear-free area over the total area of a surface has mainly determined the reduction in skin friction and the increase in slip velocity. A virtually patterned hydrophobic surface was generated with proper mesh density and surface randomness manipulations, preventing overlapping and reaching the desired gas fraction. The flow condition in their analytical approach is a steady, incompressible, laminar flow in a microchannel with the superhydrophobic surface at the bottom. In terms of the slope of the pressure gradient, it is lower for the superhydrophobic surface than for the smooth wall, which generally explains the shear-free area indeed lowered the resistance to flow. The slip lengths based on Navier's model were determined and in good agreement with the previous experimental study conducted by Lee et al. [32]Slip lengths were compared under a certain gas fraction of 0.865 and a Reynolds number of 11.85 for randomly distributed and staggered arrangement posts, showing a less pressure drop for the random distribution than the staggered one. However, more pressure drops took place in randomly distributed posts superhydrophobic surface than the staggered with increasing gas fraction. For less resistance, the flow is more likely to seek large passages in the random distribution as the path will be enlarged in a higher gas fraction. Even though the general drag reduction indicated by the randomly distributed is increasingly more remarkable than the staggered with increasing gas fraction, with the consideration of the transition threshold of the air-liquid interface into account, also defined as the maximum allowable pressure, the randomly distributed posts superhydrophobic surface cannot withstand the pressure as much as the staggered does as demonstrated in Figure 11. Thus, it affirms the significance of organized arrays of regular patterns to the system's overall drag reduction performance to maintain hydrophobicity under the maximum allowable pressure.

Durability, as one of the most significant parameters that define whether a system is stable, can be measured by an optical method to verify its longevity. Moreover, the longevity test mainly focuses on systems submerged in water, where the air will dissolve in water and pace up with increased hydrostatic pressure. Similar techniques, utilizing a light source and measuring the reflective shining spots on a substrate that represents each air bubble that corresponds to the liquid-air interface, were adopted in many experiments [33]–[36]. Samaha et al. have conducted a longevity experiment for an electrospun fibrous coating via optical spectroscopy, in which the reflective light intensity was captured at different wavelengths. It indicates a 27% decrease in drag reduction effect after 166.5 hours of immersion of the specimen in water, only a 4% difference compared to the other measuring technique, the rheometer, meaning that the optical method is acceptable. In addition, static measurement of contact angles and the hysteresis was collected, which validates the results obtained from the light-scattering technique. However, the mechanical characteristics and geometry of the structure for patterning related to the maximum allowable pressures and its durability were not specified due to the randomness of roughening fabrication. The sturdiness and the ability to maintain hydrophobicity under pressures have became a critical measurement for hydrophobic surface design [15].
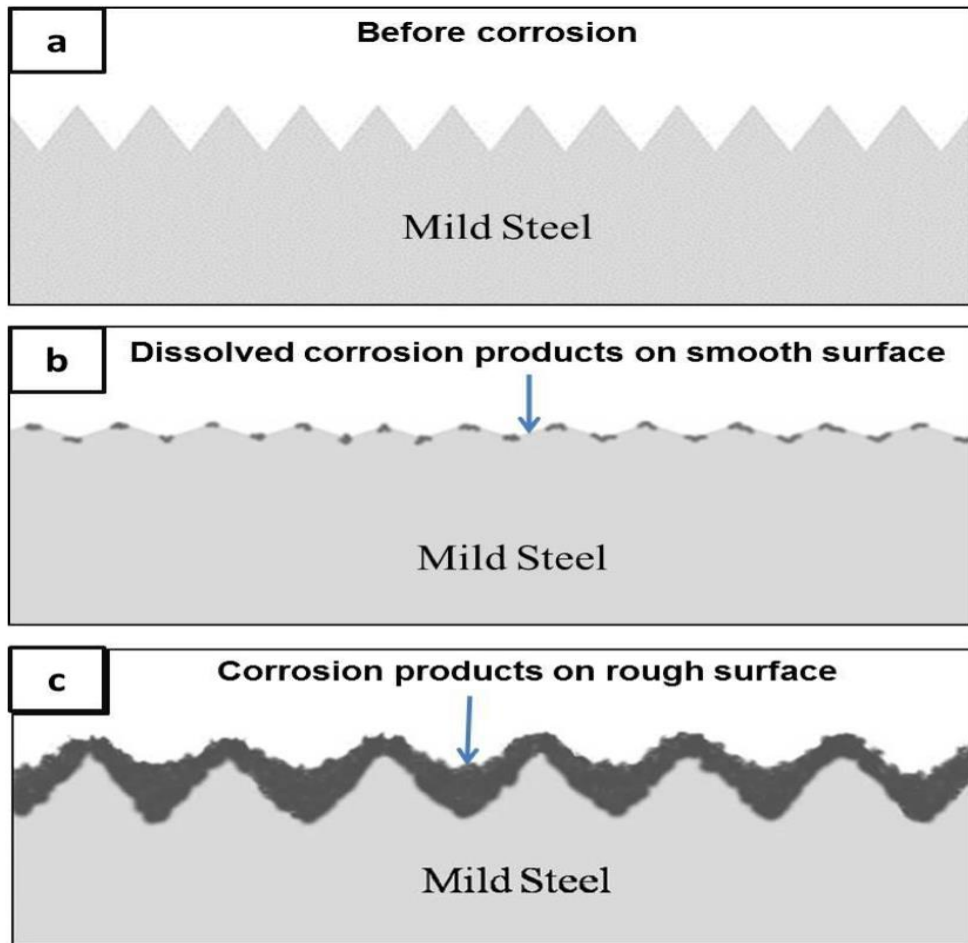
FIGURE 10. SCHEMATIC OF UNIDIRETIONALLY PATTERNED MILD STEEL SUBSTRATE. A) PRIOR TO CORROSION, B) CORRODED SMOOTH SURFACE AND C) PATTERNED SURFACE AFTER CORROSION

2.4 Corrosion Resistance

Another benefit of specific mechanically modified metal surfaces is to possess the ability to resist corrosion. After a certain deployment period, the most common change present is the corrosion on metal surfaces. Some metallic elements may form a passivated film to counter the corrosives, while the mild steel is not capable of forming such a protective layer. Unidirectional patterned mild steel and Nickel (able to form a passivated layer) substrates were experimented for their corrosion behavior conducted by Toloei, A.

[21]. The patterned mild steel surfaces demonstrated better corrosion resistance comparing that of a smooth, unpatterned surface shown in Figure 10. Similar behavior was also observed by Alvarez for the AE44 Magnesium alloy [37] There are two main reasons for the enhancement of corrosion resistance for patterned surfaces. First is the reduction in the overall solid/electrolyte contact area. Second, the air/solid interface between two neighboring asperities prevents the passivated layer from dissolving in the corrosives. In addition, patterned surfaces with grooves and valleys can restrain the diffusion of the corrosives and the corroded products within the cavity and entrap the ion, which contributes to a lower corrosion rate concerning the overall surface. Moreover, there is an optimal spatial pattern density for the mild steel substrate, where the corrosion is at its minimum. However, the corrosion rate would increase with the greater roughness of the patterned Nickel substrate. Various shapes of patterns and fabrication methods were suggested that are in need to be verified regrading corrosion resistance, which would propagate the investigation of more comprehensive aspects of mechanically modified surfaces [21] .

2.5 Applications of Superhydrophobic surfaces

Superhydrophobic surfaces and their behavioral characteristics have been studied for decades, whereas industrial applications are still constrained due to fabrication techniques, cost, effectiveness, durability and many other aspects. In contrast, the chemical passivated superhydrophobic applications can be utilized in water-repellant products for clothing and short-term self-cleaning (waxing) for painting cosmetics on metal surfaces.

In the automotive industry, surface patterning has been deployed onto the cylinder bores of the combustion engine [38]. And part of the engine block utilizes the nitride silicon

ceramic plates modified with micro asperities for abrasive contact with cylinder heads [39]. Despite the shapes of texturee, A typical abrasive test, the pin-on-disk, was conducted to examine the coefficient of friction in boundary and mixed lubricating scenarios. The achievement in coefficient reduction is 20% with $100\mu m$ of geometry size and density of 5 to 20%. Sealing rings that have been laser textured contribute to a reduction in overall engine friction of 30%[40]–[43]. Similar amount of friction reduction was also detected in that of the cylinder liner. In Micro-electromechanical systems, surface patterning is generally adopted for controlling the roughness regarding adhesion and friction [44]. With greater roughness of a patterned surface, the coefficient of friction and pulling force were less presented in experiments [44], [45]. The static pressure soars up on patterned surface due to the reduced actual contact area with the same number of external forces comparing to a smooth surface, which will enhance the stiffness of a tool fixture [46]. PolyMUMPs is widely used in micro/nano-chips fabrication, where the topography resembles the characteristics of the asperities on a patterned surface, which is considered as an optional method for experimenting hydrophobic surface designs.

2.6 Objectives

With the comprehensive revision of the mechanism, fabrication methods, tribological characteristics, and performance parameters for (super)hydrophobicity on metal substrates, the geometry of mechanical surface patterning design is still in the urge to be investigated to achieve a more sturdy, stable, and endurable structure. Existing studies have mainly worked on providing a hybrid, chemically coated and patterned fabrication method to obtain super hydrophobicity.

The main objective of this thesis is to propose a novel superhydrophobic system design that can endure a certain amount of external pressure that is extra to the atmospheric pressure. The design is naturally inspired by the hierarchical and multi-scale structures on the lotus leaf. By incorporating "undercut" like contours on the cross-sectional profile, the re-entrant curvature can benefit the system's stability to lower the localized surface energy. A two-stage "undercut" flat-top-pillar design is analytically studied. Also, given the most feasible and optimal undercut permutations from the analytical approach, numerical analysis is conducted in COMSOL Multiphysics, in which the maximum allowable extra pressures of each design are found. The comparison of each design with their corresponding pair of undercut angles is carried out in the individual maximum allowable extra pressure. The 2-Dimensional volume fraction of the fluid diagram visualized and monitored the whole transition process from heterogeneous to homogeneous wetting for each designed system. The polysilicon method's chosen fabrication aimed to satisfy the proof-of-concept because of its bottom-up layer-by-layer depositing techniques with increments in size for the successive layer. In addition, rectangular, circular and hexagonal shapes of asperities are prepared for future experiments regarding sliding and other abrasive tests. Each specimen will be placed in a pressurized chamber and monitored the contact angle with water droplet via the goniometer.

CHAPTER 3 THEORY AND ANALYTICAL ANALYSIS

3.1 Theory

For any shape of protrusion on a flat surface, the change in hydrophobicity can be identified and studied by the derivation of the Gibbs free energy. In addition, the assumption of the system is that the protrusions are cylindrical in their z-axis while primarily focusing on the cross-sectional view of the protrusions themselves [47]. When the system encounters liquid, the corresponding Gibbs free energy can be generally written as:

$$G = \gamma_l A_l + \gamma_s A_s + \gamma_{ls} A_{ls}, \qquad \text{Eq.5}$$

where γ is the surface tension, A is the surface area, and the subscripts s and l represent solid and liquid, respectively. The correlation of Young contact angle (Eq.1) with Eq.5 yields:

$$G = \gamma_l (A_l - A_{sl} \cos(\theta)) + \gamma_s (A_s + A_{ls}), \qquad \text{Eq.6}$$

To be more specific, the dynamic scenario of the system would only be the transition/variation of wetting, omitting the variables of the solid side, leaving as:

$$\Delta G = \gamma_l (\delta A_l - \delta A_{sl} \cos(\theta)), \qquad \text{Eq.7}$$

To investigate this dynamic behaviour of the transition of wetting, a quasi-static/meta-stable state exhibits the equilibrium of the system, where can be met at the minimum of the Gibbs free energy:

$$\Delta G = 0, \qquad \text{Eq.8}$$

For later fabrication (typically limited to simple protrusion shapes), symmetrical and linear profiles with sharp inflection points will be discussed for further analysis.

Looking at this particularly shaped structure shown in Figure 6, the linear slope on either side of the structure can yield:

$$f_1'(x) = const. \quad \text{and thus,} \quad f_1''(x) = 0 \qquad \text{Eq.9}$$

where $z = f(x)$ represents the surface of the structure. For a stable heterogeneous wetting scenario of this type of system to exist, the boundary condition at the tips of this flat-top-pillar structure contributes to a minimum energy state while assuming the Gibbs free energy function is continuous [47] Moreover, for such an inherently hydrophilic surface (e.g., $cos\theta > 0$), the particular condition shown in Eq.10 must be satisfied for displaying heterogeneous wetting (Cassie-Baxter wetting).

$$\alpha_1 < \alpha_2, \qquad \text{Eq.10}$$

A structure satisfying Eq.10 will have a broader lower part and a narrower upper part (Figure 11). Such structure will be referred to as an "undercut" structure.
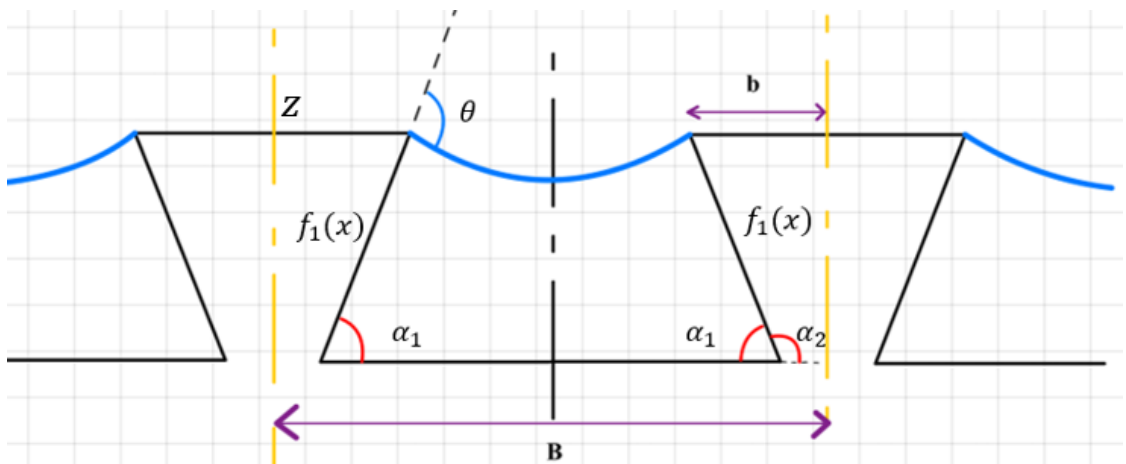
FIGURE 11 CROSS-SECTIONAL SCHEMATIC OF A LINEAR SHAPED, FLAT TOP, CYLINDRICAL IN Z-AXIS PILLAR.

To examine the performance of a patterned surface, it is to eventually find the path to the most stable state (Wenzel state, homogeneous wetting). In terms of the Gibbs free energy, the equilibrium state of a system might not be at the lowest level of energy, while there is a certain threshold that states the global minimum of this energy level. Then, rewrite Eq. 6 into the following:

$$\Delta G = G - G^{bot} = \gamma_l(A_l - A_l^{bot} - (A_{sl} - A_{sl}^{bot})cos\theta), \qquad \text{Eq.11}$$

where $\delta\Delta = A_{sl} - A_{sl}^{bot}$. If we use that for complete wetting, $A_l^{bot} = 0$ we obtain,

$$\Delta G = \gamma_1(A_l - \delta A_{sl}cos\theta), \qquad \text{Eq.12}$$

As the liquid/air interface propagates (wets) along the sidewalls of the structure, $A_{sl}^{bot} > A_{sl}$, and thus,

$$\Delta A_{sl} = A_{sl} - A_{sl}^{bot} < 0, \qquad \text{Eq.13}$$

$$A_l > 0,$$

By rearranging, Eq.11 can be written as:

$$\Delta G = \gamma_l(|A_l| + |\Delta A_{sl}|cos\theta), \qquad \text{Eq.14}$$

Consequently, it leaves the inherent contact angle θ as the only factor that determines whether the system favors a homogenous or heterogeneous wetting. With the inherent contact angle $\theta < 90°(cos\theta > 0)$, the corresponding value of ΔG is positive, and the system favors homogeneous wetting rather than maintaining the liquid/air interface at a certain local minimum. On the contrary, if the inherent contact angle $\theta > 90°(cos\theta < 0)$, meaning a naturally "phobic" surface, the system favors heterogenous wetting.

Nevertheless, surfaces with an inherent contact angle of smaller than 90 degrees can experience heterogeneous wetting if appropriately patterned, even if the ultimate stable state is complete wetting at a global minimum in its energy level. Even so, with certain conditions, such as extra forces/pressures, or certain fluid velocity, being satisfied, the system can encounter a transition from a heterogeneous wetting to a homogeneous one owing to breaching the potential barrier between the local minimum and the global one.

3.2 Linear pillars and general patterns

The selection of flat-top-pillar symmetric system is one of the multiple variants of systems that satisfy Eq10. Further discussion of other available linear systems, regardless of fabrication barriers, is presented in this section.

The sidewalls ($z = f_1(x), f_2(x)$) describe the profiles of two neighboring protrusions, and their relationships with the angles at the lower inflexion points shown in Figure 6. can be written as:

$$f_1'(x) = \tan(\alpha_1), \qquad \text{Eq.15}$$

$$f_2'(x) = \tan(\alpha_2).$$

For any arbitrary shapes of protrusion, the corresponding change in the Gibbs free energy equation affected by the change in location of the liquid surface (δz) is:

$$\frac{\delta G}{L\gamma_l\delta z} = -\left(\frac{1}{f_1'(x)} - \frac{1}{f_2'(x)}\right) + \left(\sqrt{1 + \frac{1}{f_2'^2(x)}} + \sqrt{1 + \frac{1}{f_2'^2(x)}}\right)\cos(\theta), \qquad \text{Eq.16}$$

If we rearrange Eq16 with respect to the equilibrium state at the local minimum of the Gibbs free energy ($\frac{\delta G}{L\gamma_l\delta z} = 0$):

$$\cos(\theta) = \frac{\frac{1}{f_1'(x)} - \frac{1}{f_2'(x)}}{\sqrt{1+\frac{1}{f_2'^2(x)}} + \sqrt{1+\frac{1}{f_2'^2(x)}}},$$

<div align="right">Eq.17</div>

Moreover, the second partial derivative of the Gibbs free energy is positive

$$\frac{\delta^2 G}{L\gamma_l \delta z \delta z} > 0,$$

<div align="right">Eq.18</div>

By incorporating $\frac{\delta}{\delta z} = \frac{1}{f_1'(x)}\frac{\delta}{\delta x}$ with Eq16 and ($\frac{\delta G}{L\gamma_l \delta z} = 0$), the following one is obtained,

<div align="right">Eq.19</div>

$$\frac{1}{f_1'^2(x)}\frac{f_1''(x)}{f_1'(x)}\left(1 - \frac{\cos(\theta)}{\sqrt{1+f_1'^2(x)}}\right) - \frac{1}{f_2'^2(x)}\frac{f_2''(x)}{f_2'(x)}\left(1 + \frac{\cos(\theta)}{\sqrt{1+f_2'^2(x)}}\right) > 0,$$

which indicates a situation where the heterogeneous wetting for any arbitrary protrusion system [47]. Thus, for inherently "philic" surfaces with contact angle less than 90° and $\cos(\theta) > 0$, the numerator of Eq17 is greater than 0.

$$\frac{1}{f_1'(x)} - \frac{1}{f_2'(x)} > 0,$$

<div align="right">Eq.20</div>

For simplicity, Eq17, 19 and 20 combined with Eq15 will result in the following equations to limit the concerned objects in inherently "philic" surfaces:

$$\cos(\theta) = \frac{\sin(\alpha_2 - \alpha_1)}{\sin(\alpha_2) + \sin(\alpha_1)},$$

<div align="right">Eq.21</div>

$$\frac{\sin(\alpha_2 - \alpha_1)}{\sin(\alpha_2)\sin(\alpha_1)} > 0,$$

<div align="right">Eq.22</div>

$$\frac{f_1''(x)}{f_1'(x)}\left(\frac{1-\cos(\theta)|\cos(\alpha_1)|}{tan^2(\alpha_1)}\right) - \frac{f_2''(x)}{f_2'(x)}\left(\frac{1+\cos(\theta)|\cos(\alpha_2)|}{tan^2(\alpha_2)}\right) > 0,$$

<div align="right">Eq.23</div>

In addition. Equation 22 also yields Eq10. And with the above mentioned eq10, 21 and 23, two coefficients (K_1, K_2) can be acquired, which defines a series of linear patterns that meet stable heterogeneous wetting criteria.

$$f_1'(x)f_2'(x)(f_1''(x)f_2'(x)K_1 - f_2''(x)f_1'(x)K_2) > 0, \qquad \text{Eq.24}$$

Where,

$$K_1 = \frac{1-\cos{(\theta)}|\cos{(\alpha_1)}|}{\tan^2{(\alpha_1)}} > 0, \qquad \text{Eq.25}$$

$$K_2 = \frac{1+\cos{(\theta)}|\cos{(\alpha_2)}|}{\tan^2{(\alpha_2)}} > 0. \qquad \text{Eq.26}$$

Based on eq10, 21 and 24, there are six main categories of patterns that will be addressed. The $f_1'(x)$ and $f_2'(x)$ for set two have the same signs as set one, which implies that set two is the mirror case of set one.

Set 1 $\boldsymbol{f_1''(x)f_2'(x)A_1 - f_2''(x)f_1'(x)A_2 > 0}$ *and* $\boldsymbol{f_1'(x) > 0, f_2'(x) > 0}$

Given $0 \leq \alpha_1 \leq 90°$ and $0 \leq \alpha_2 \leq 90°$, the accordance of $f_1'(x) = tan(\alpha_1)$ and $f_2'(x) = tan(\alpha_2)$ with eq10 results in $f_1'(x) < f_2'(x)$, and correspondingly $f_1''(x) > f_2''(x)\frac{f_1'(x)A_2}{f_2'(x)A_1}$. By meeting the above criteria, there are two sets of patterns illustrated in Figure 12 (a & b) and Figures 13 (a & b), respectively.

(a)   (b)
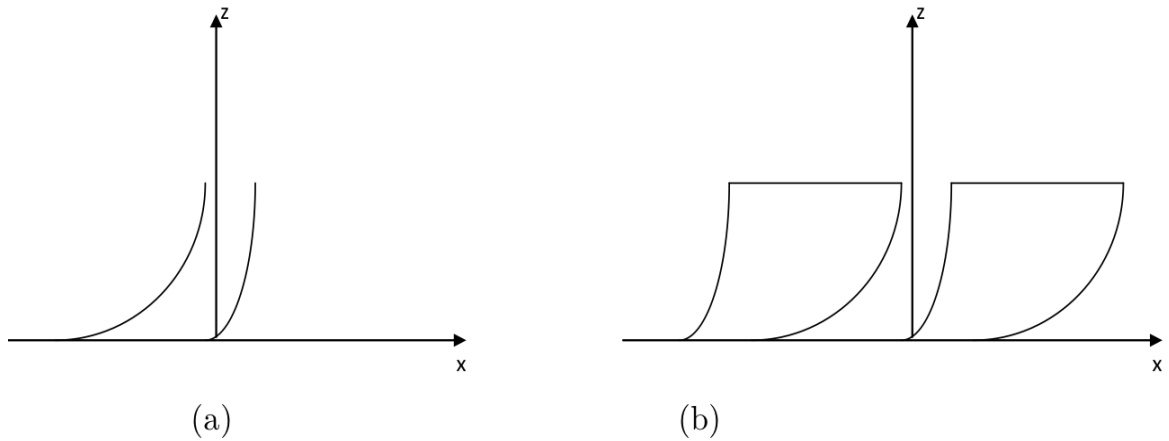
FIGURE 12. SCHEMATICS OF THE SIDE PROFILES A) FOR SET 1, AND THEIR ENCLOSED LAYOUT B).

Set 2 $f_1''(x)f_2'(x)A_1 - f_2''(x)f_1'(x)A_2 > 0$ *and* $f_1'(x) < 0, f_2'(x) < 0$

(a)

(b)
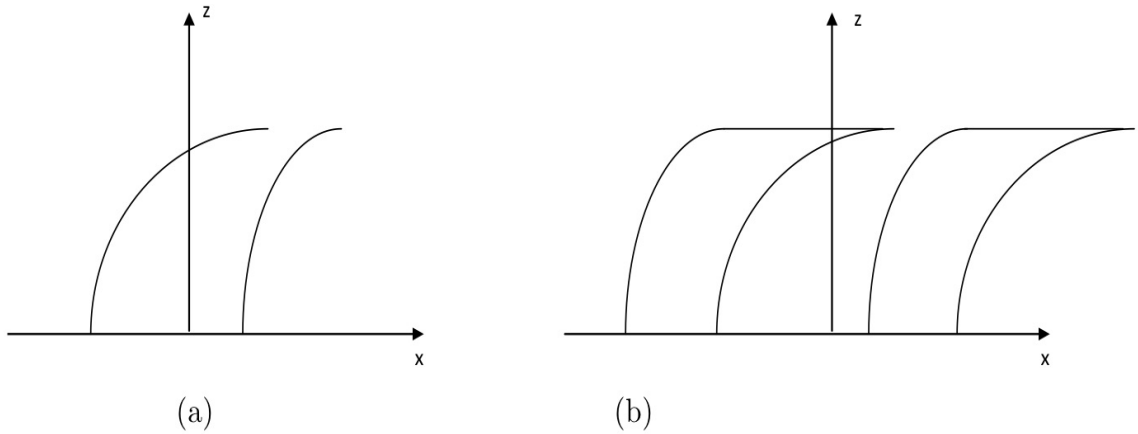
FIGURE 13. SCHEMATICS OF THE SIDE PROFIES A) FOR SET 2, AND THEIR ENCLOSED LAYOUT B).

The relative schematics are Figures 8 (a & b), which are mirrored from set 1.

Set 3 $f_1''(x)f_2'(x)A_1 - f_2''(x)f_1'(x)A_2 < 0$ *and* $f_1'(x) > 0, f_2'(x) < 0$

This curvilinear shape can be satisfied under many circumstances, such as cylindrical and semi-cylindrical. The related α_1 and α_2 range from 0 to 90°, and 90° to 180° , respectively. Plus, a particularly coupled angles α_1 and α_2 exist and meet the requirement for eq21. Relative schematics are presented in Figure 14 (a & b), Figure 14 (a & b), and Figure 16 (a & b).

(a)

(b)
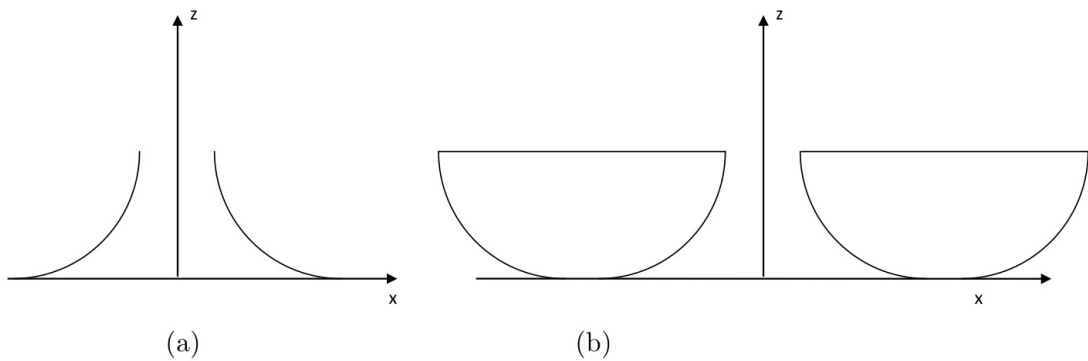
FIGURE 14. SCHEMATICS OF THE SIDE PROFIES A) FOR SET 3, AND THEIR ENCLOSED LAYOUT B).

27

(a)   (b)
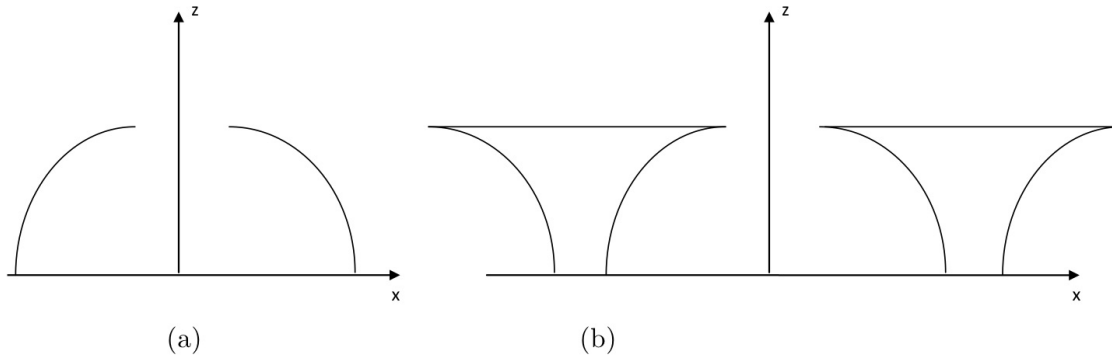
FIGURE 15. SCHEMATICS OF THE SIDE PROFIES A) FOR SET 3, AND THEIR
ENCLOSED LAYOUT B).

(a)   (b)
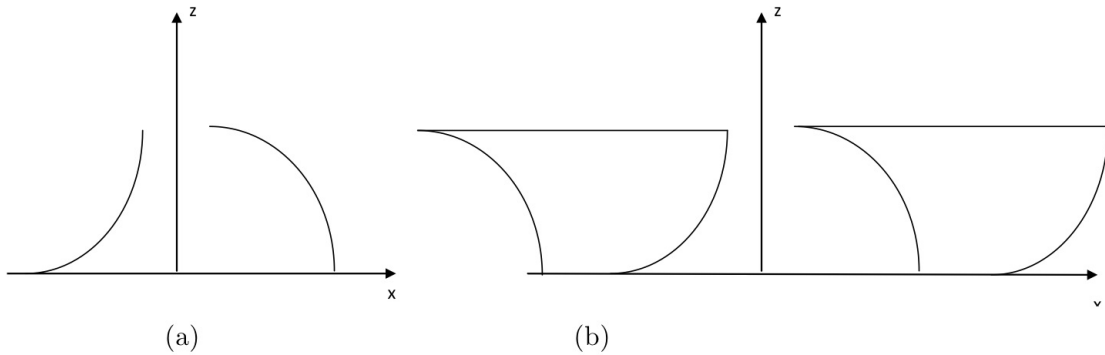
FIGURE 16. SCHEMATICS OF THE SIDE PROFIES A) FOR SET 3, AND THEIR
ENCLOSED LAYOUT B).

Set 4 $f_1''(x)f_2'(x)A_1 - f_2''(x)f_1'(x)A_2 < 0$ *and* $f_1'(x) < 0, f_2'(x) > 0$

The disobedience of this condition with eq10 will not grant hydrophobicity to this

type of configuration.

Set 5 $f_1''(x)f_2'(x) < 0$ *and* $f_1'(x) = \infty$

This type of configuration resembles the shape of the hair-like structure on the lotus

leaf shown in Figure 17.
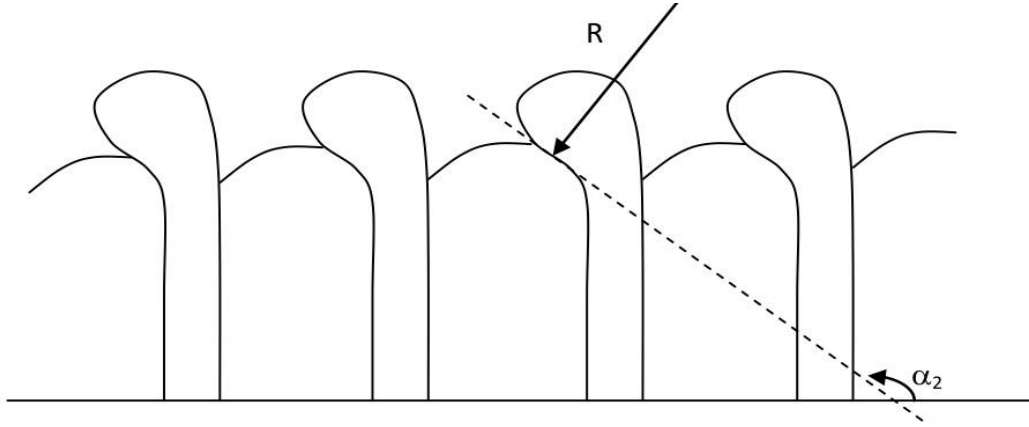
FIGURE 17. SCHEMATICS OF THE PATTERNS FOR SET 5.

Set 6 $f_1''(x)f_2'(x) > 0$ and $f_2'(x) = \infty$

The side profiles and patterns of this particular type of configuration are the mirrored image of Set 5.

3.3 The Symmetric Flat-top-pillar Design

Various studies have demonstrated that the symmetry of a geometry (Figure 6) on a patterned surface could provide a stabilized Cassie-Baxter wetting condition. For such a configuration, the relationship between angle α_1 and α_2 can be addressed as:

$$\alpha_2 = 180° - \alpha_1 \qquad \text{Eq.27}$$

Consequently,

$$f'(x) = f_1'(x) = -f_2'(x) \qquad \text{Eq.28}$$

So that corresponding curvatures are:

$$f''(x) = f_1''(x) = f_2''(x), \qquad \text{Eq.29}$$

Thus, several conditions influenced by Eq27, 28, and 29 are obtained as the followings under the assumption of an inherently "philic" surface:

Two separate types of asperities with convex (if $f''(x) < 0 \ and \ f'(x) > 0$) and concave (if $f''(x) < 0 \ and \ f'(x) < 0$) shapes are presented in Figure 18 (a & b), which are respectively.

(a)   (b)
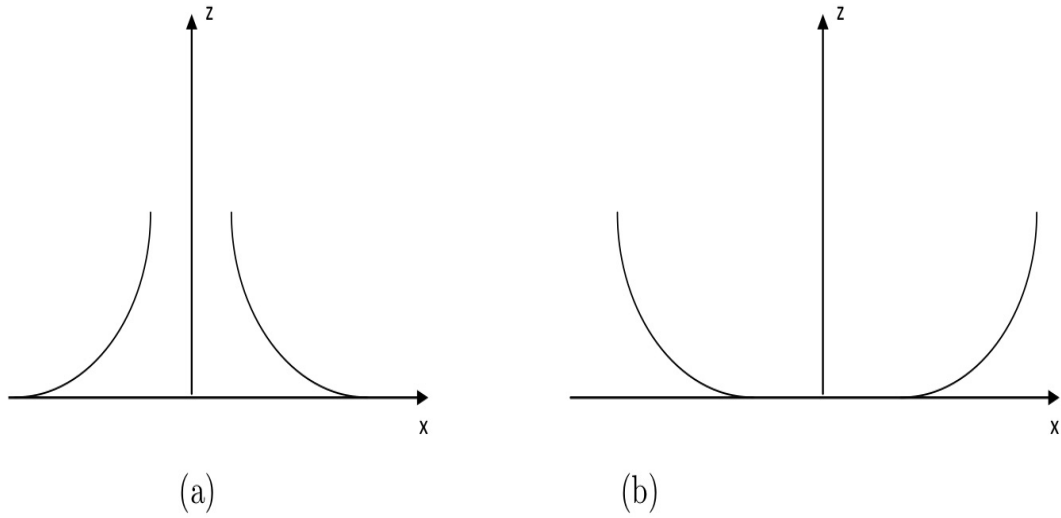
FIGURE 18. SCHEMATICS OF THE SIDE PROFILES OF A) CONVEX AND B) CONCAVE.

$$\theta = \alpha_1 \, , \qquad\qquad\qquad \text{Eq.30}$$

$$\alpha_1 < 90° \, , \qquad\qquad\qquad \text{Eq.31}$$

$$\frac{f''(x)}{f'(x)} > 0 \qquad\qquad\qquad \text{Eq.32}$$

With a flat-top feature for any asperities, it is beneficial to fabricate a mechanically modified method. Still, the calculation of the actual contact area for the substrate is also more convenient. A particular configuration with flat-top and undercut features is presented in Figure 19. The "phobic" criterion for this type of system can be established if the below equations are satisfied.
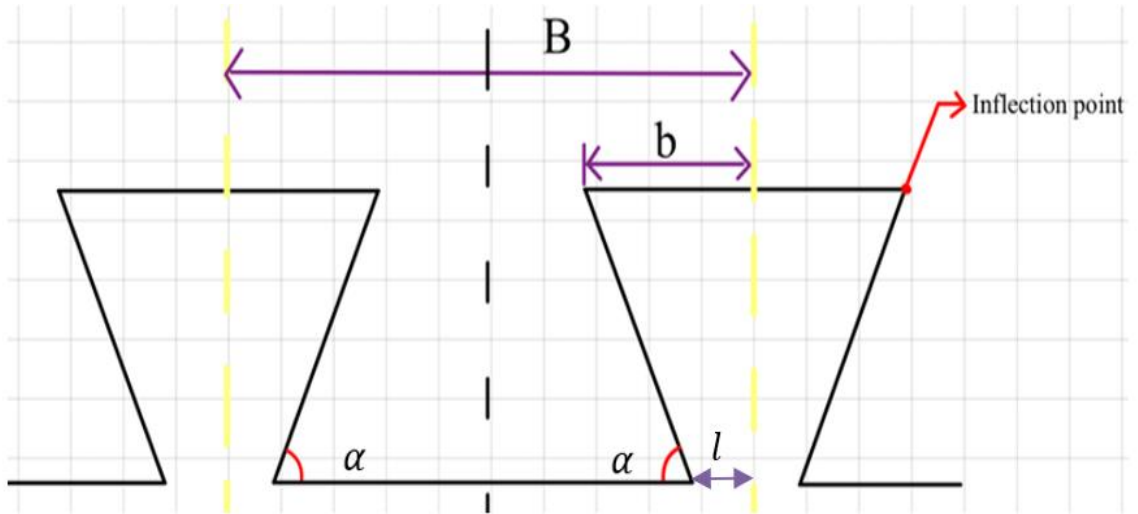
FIGURE 19. CROSS-SECTIONAL SCHEMATIC OF A SINGLE UNDERCUT FLAT-TOP-PILLAR STRUCTURE

Considering the geometry of the single undercut structure is a protrusion type one with a narrowing width from top to bottom, the two determinant factors of the height of an undercut structure are center-to-center (central axis of structure) distance (B) and inflection point-to-center distance (b) labeled in Figure 19, as they would affect the side profile aspect ratio of the undercut structure. Therefore, the fractions of areas per unit projected areas for liquid-solid (λ_{ls}) and liquid-gas (λ_{lg}) interfaces are:

$$\lambda_{ls} = \frac{2b}{B} \qquad \text{Eq.33}$$

$$\lambda_{lg} = (1 - \lambda_{ls}) \frac{\theta - \alpha}{\sin(\theta - \alpha)} \qquad \text{Eq.34}$$

The estimation equation eq 35 for the apparent contact angle is rearranged after the substitution of eq 33 and 34.

$$\cos(\theta_A) = \frac{2b}{B} \cos(\theta) - (1 - \frac{2b}{B}) \frac{\theta - \alpha}{\sin(\theta - \alpha)} \qquad \text{Eq.35}$$

So that an "phobic" surface is observed for $\cos(\theta_A) < 0$ if

$$B > 2b(1 + \cos(\theta)) \frac{\sin(\theta - \alpha)}{\theta - \alpha} \qquad \text{Eq.36}$$

In general, the hydrophobicity is obtainable for a symmetric flat-top-pillar configuration if Eq30 (or $\alpha < \theta$)and Eq 36 are satisfied at the same time.

3.4 Stability of a flat-top-pillar system

With the consideration of practicality, $\theta > \alpha$ will be considered as the flat-top-pillar system does not acquire a local minimum in energy. Hence, two globally stable states for the liquid-air interface reside at the inflection point and the bottom of the valley where it touches the bulk substrate. Moreover, the homogenous wetting (substrate entirely wetted) represents the global minimum which obtains the most stable state. The transition for the liquid-air interface from the inflection point to the substrate's bulk surface would require a certain amount of energy to achieve. This energy acquisition from the flection point to the substrate's bulk surface (maximum Gibbs free energy) is consequently the change in the

Gibbs free energy mentioned in Section 3.1. For this specific configuration, the maximum change in the Gibbs free energy becomes:

$$\Delta G^{max} = G^{max} - G^{top} = \tau_l\left(A_l^{max} - A_l^{top} - (A_{sl}^{max} - A_{sl}^{top})\cos(\theta)\right) \qquad \text{Eq.37}$$

To specify the areas, depth z is introduced for the liquid-air surface to approach the substrate's bulk surface, which obtained the following:

$$A_l - A_l^{top} = \frac{2(H-z)L}{\tan(\alpha)\cos(\theta-\alpha)} \qquad \text{Eq.38}$$

$$A_{sl} - A_{sl}^{top} = \frac{2(H-z)L}{\sin(\alpha)} \qquad \text{Eq.39}$$

The product after the substitution of eq38 and 39 to eq 37 is:

$$\Delta G = G - G^{top} = \frac{2(H-z)\tau_l L}{\sin(\alpha)}\left(\frac{\cos(\alpha)}{\cos(\theta-\alpha)} - \cos(\theta)\right) \qquad \text{Eq.40}$$

The substrate's bulk surface, where the liquid-air surface is in proximity, sits at $z = 0$; therefore, ΔG^{max} is obtained when $z = 0$ in the case of $\theta > \alpha$. In addition, the mandatory(minimum) change in the Gibbs free energy from heterogeneous to homogeneous wetting is determined as:

$$\Delta G^{min} = G^{max} - G^{top} = \frac{2H\tau_l L}{\sin(\alpha)}\left(\frac{\cos(\alpha)}{\cos(\theta-\alpha)} - \cos(\theta)\right) \qquad \text{Eq.41}$$

The undercut angle α and ΔG are inversely related to each other. To interpret the corresponding pressure required for the wetting transition, the Gibbs free energy needed to push the liquid-air interface to a certain volume V is:

$$\Delta G^p = V\Delta p = \left(B - 2b - \frac{H}{\tan(\alpha)}\right)L\Delta p \qquad \text{Eq.42}$$

The condition where the transition would have taken place is:

$$\Delta G^p \geq \Delta G^{min} \qquad \text{Eq.43}$$

which leads to the evaluation of the stability factor, extra pressure Δp, of this type of configuration, where

$$\Delta p \geq \frac{2H\tau_l}{(B-2b)\sin(\alpha) - H\cos(\alpha)}\left(\frac{\cos(\alpha)}{\cos(\theta-\alpha)} - \cos(\theta)\right), \qquad \text{Eq.44}$$

The denominator determines that:

$$(B-2b)\tan(\alpha) > H \qquad \text{Eq.45}$$

For the later evaluation of the single-undercut angle and novel double-undercut angle flat-top-pillar designs, both Eq36 and 44 will be utilized to obtain the hydrophobicity check and maximum extra pressure.

3.5 Sizing of the single-undercut structure

The verification process of the improvement for double-undercut flat-top-pillar designs is crucial for many reasons. First of all, the dimension in the structure's height, whether it is a single or double undercut design, plays an important role when measuring the maximum allowable pressure while having both systems satisfy the hydrophobic character. Another distinct consideration is the undercut angles, which can affect the width of each stage of the structure. Furthermore, the selection of two undercut angles, whether feasible for such a double-undercut design, matters significantly.

The geometry shown in Figure 19 of the single undercut structure is a protrusion type one with a narrowing width from top to bottom, which obeys the aforementioned

34

hydrophobicity in Eq44. The two determinant factors of the height of an undercut structure are center-to-center (central axis of structure) distance (B) and inflection point-to-center distance (b) labeled in Figure 19, as they would affect the side profile aspect ratio of the undercut structure correspondingly. In addition, the feasibility of fabrication needs to be taken into account for sizing parameters. The range between nano and micro-scales is favored by most adopted fabrication methods in the industry, such as micro-machining, photolithography, and laser ablation. Plus, according to condition $\theta > \alpha$, which is exclusive to the flat-top-pillar configuration, the undercut angle required should be lower than the inherent water contact angle of a substrate made from a specific material (chemical composition). With the choice of PolyMUMPs for later fabrication, where the structure will be manipulated on a silicon wafer, the value for $\theta = 53.5°$. Thus, three different groups of data sets regarding undercut angles ranging from 50 to 36 degrees are presented in the table below. The upper limit of undercut angle of 50 degrees was selected as it should always be less than the inherent contact angle of water on the flat surface. At the same time, the lower limit of undercut angle is 36 degrees for the consideration of later fabrication feasibility.

Table 1 shows that the minimum aspect ratio of set 1 is 1.25, namely the fraction of 2 times b over H of the undercut angle 50 degrees when looking at the cross-sectional profile of the undercut structure. The gap between the two inflection points is (B-2b), which consequently results in the magnitude of the height H. One thing to notice is that the heights listed in the tables are chosen as much as close to $(B - 2b)\tan(\alpha)$; meanwhile, to keep

the denominator as small as possible for the larger output of the calculated extra pressure, 99.99999% of the calculated $(B - 2b) \tan(\alpha)$ is equivalent to height H.

α (deg)	B (μm)	b (μm)	H (μm)
	Set 1		
50	500	150	238.35071852
49	500	150	230.07368144
48	500	150	222.12250297
47	500	150	214.47374200
46	500	150	207.10606276
45	500	150	200.00000000
44	500	150	193.13775496
43	500	150	186.50301723
42	500	150	180.08080886
41	500	150	173.85734756
40	500	150	167.81992624
39	500	150	161.95680664
38	500	150	156.25712530
37	500	150	150.71081002
36	500	150	145.30850560

Table 1 HEIGHTS DERIVED FROM DESCENDING UNDERCUT ANGLES (50 TO 36DEGREE) FOR B=500 MM, B=150 MM. MINIMUM ASPECT RATIO = 1.25

Same rules and disciplines are applied to Set 2 and Set 3, indicated in Tables 2 and 3, with the exact resolution of the calculated heights, where the differences between every two sets are the distancing of two asperities and heights, which are the aspect ratios. The most significant aspect ratio is achieved at 2.51 for Set 3 among these three sets, meaning that the larger the aspect ratio, the less chance of necking on the asperities may happen when the substrate is encountering abrasive forces or external pressures.

	Set 2		
α (deg)	B(μm)	b(μm)	H(μm)
50	1000	250	595.87679630
49	1000	250	575.18420361
48	1000	250	555.30625741
47	1000	250	536.18435501
46	1000	250	517.76515690
45	1000	250	500.00000000
44	1000	250	482.84438740
43	1000	250	466.25754307
42	1000	250	450.20202215
41	1000	250	434.64336891
40	1000	250	419.54981559
39	1000	250	404.89201660
38	1000	250	390.64281325
37	1000	250	376.77702505
36	1000	250	363.27126400

Table 2 HEIGHTS DERIVED FROM DESCENDING UNDERCUT ANGLES (50 TO 36DEGREE) FOR B=1000 MM, B=250 MM. MINIMUM ASPECT RATIO = 0.83

	Set 3		
α (deg)	B(μm)	b(μm)	H(μm)
50	1200	450	357.52607778
49	1200	450	345.11052217
48	1200	450	333.18375445
47	1200	450	321.71061301
46	1200	450	310.65909414
45	1200	450	300.00000000
44	1200	450	289.70663244
43	1200	450	279.75452584
42	1200	450	270.12121329
41	1200	450	260.78602134
40	1200	450	251.72988935
39	1200	450	242.93520996
38	1200	450	234.38568795
37	1200	450	226.06621503
36	1200	450	217.96275840

Table 3 HEIGHTS DERIVED FROM DESCENDING UNDERCUT ANGLES (50 TO 36DEGREE) FOR B=1200 ＭM. B=450 ＭM. MINIMUM ASPECT RATIO =

In addition, the extra pressures were obtained using Eq44 demonstrated in Table 4, 5, and 6. The obtained average values for the extra pressure of each set satisfied and exceeded the expectancy, which is one-third of the atmospheric pressure.

Set1				
α (deg)	B(μm)	b(μm)	3 digits after decimal point of 99.99999% H	δP (Pa)
50	500	150	238.350	3653.732904
49	500	150	230.073	4688.326026
48	500	150	222.122	7356.314715
47	500	150	214.473	5589.631691
46	500	150	207.106	72397.21214
45	500	150	199.999	4893.0862
44	500	150	193.137	6888.971475
43	500	150	186.503	317572.8896
42	500	150	180.080	7055.417445
41	500	150	173.857	17008.84907
40	500	150	167.819	6572.955825
39	500	150	161.956	7734.183946
38	500	150	156.257	50802.03779
37	500	150	150.710	7988.099523
36	500	150	145.308	12965.44455

Table 4 RESULTS OF THE CALCULATED EXTRA PRESSURES FOR SET 1

Set2				
α (deg)	B(μm)	b(μm)	3 digits after decimal point of 99.99999% H	**δP (Pa)**
50	1000	250	595.876	8242.15084
49	1000	250	575.184	39227.3586
48	1000	250	555.306	35934.0701
47	1000	250	536.184	29207.0544
46	1000	250	517.765	72397.2121
45	1000	250	499.999	12232.7522
44	1000	250	482.844	33562.7021
43	1000	250	466.257	25185.5338
42	1000	250	450.202	644147.352
41	1000	250	434.643	40061.8567
40	1000	250	419.549	18661.7561
39	1000	250	404.892	939708.372
38	1000	250	390.642	19568.1806
37	1000	250	376.777	645728.376
36	1000	250	363.271	62076.6492

Table 5 RESULTS OF THE CALCULATED EXTRA PRESSURES FOR SET 2

Set3				
α (deg)	B(μm)	b(μm)	3 digits after decimal point of 99.99999% H	**δP (Pa)**
50	1200	450	357.526	50630.1474
49	1200	450	345.11	9177.642826
48	1200	450	333.183	7356.314714
47	1200	450	321.71	10148.83521
46	1200	450	310.659	72397.21213
45	1200	450	299.999	7339.641532
44	1200	450	289.706	12335.31839
43	1200	450	279.754	15606.38388
42	1200	450	270.121	40134.65496
41	1200	450	260.786	415439.1215
40	1200	450	251.729	10268.33367
39	1200	450	242.935	44571.09405
38	1200	450	234.385	13879.34739
37	1200	450	226.066	45136.92209
36	1200	450	217.962	12965.44455

Table 6 RESULTS OF THE CALCULATED EXTRA PRESSURES FOR SET 3

3.6 Sizing of the double-undercut design

The comparison between the single and double-undercut designs needs to limit as many variables as possible to pursue the extent of enhancement by design itself. Thus, restraining the dimension, especially the overall height of each design, is crucial to the simulation process. The double-undercut design would have to possess two stages with two different undercut angles, respectively, while the overall height is the same as that of the single-undercut design with a greater undercut angle from the chosen two. For structural stability and avoidance of necking phenomenon potentially caused by abrasive forces to the patterned substrate, the overall height is split into two equal sections. The placement and order of the two stages can be differentiated into two cases regarding the distancing of the inflection points of two neighboring structures. Case 1, a wider top opening means a greater distance between inflection points of two neighboring structures at the first stage than that of the second as illustrated in Figure 20. As for a wider bottom opening, Case 2,
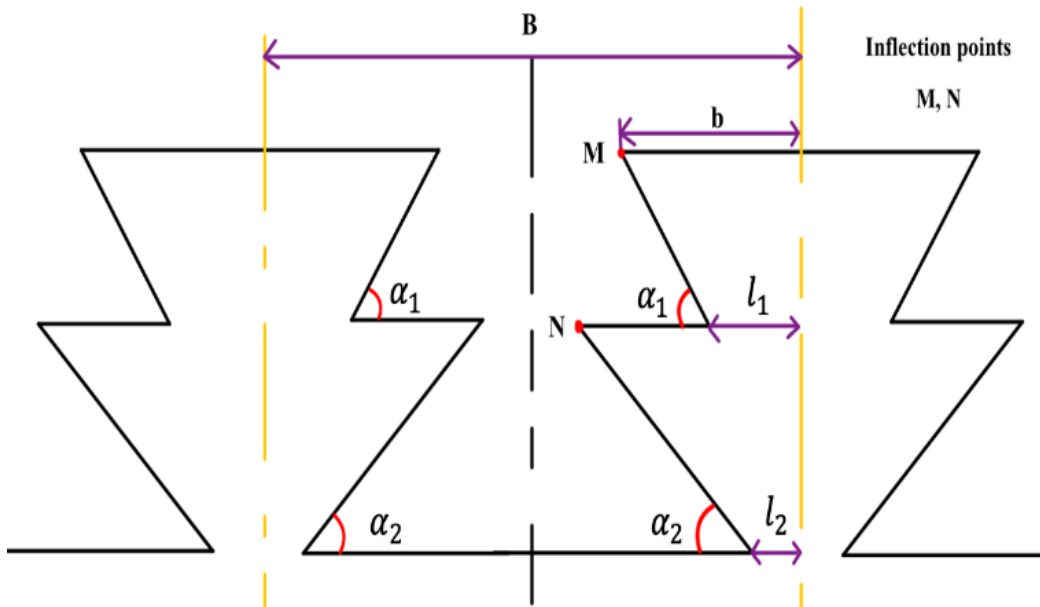

FIGURE 20.   SCHEMATICS OF A WIDER TOP OPENING DOUBLE-
UNDERCUT DESIGN

the greater distancing is at the second stage.

The extra calculation for the double-undercut designs remains the same procedure once the overall height has been properly distributed to each stage. Scale-wise, three different scales based on the value of "B", namely B=1200,800, and 400μm, were selected to calculate the undercut angle's combination for 50 and 40 degrees in two opposite angle placement cases. The detailed dimensions and results are shown in Table 7. Each extra pressure presented is the sum of that of each stage for the double-undercut design based on the hypothesis of simple addition.

Extra Pressure of the Double-undercut for three different scales (50 and 40 degree)			
B (μm)	1200	800	400
Height H(μm)	357.526	238.351	119.175
Extra Pressure Case 1(Pascal)	**993,408**	**12,747,574**	**12,747,569**
ℓ1(μm)	280.437	186.985	93.479
ℓ2(μm)	375.000	250.000	125.000
Extra Pressure Case 2(Pascal)	**675,124**	**142,767**	**156,890**
ℓ1(μm)	450.000	255.000	110.000
ℓ2(μm)	173.917	165.654	114.782

Table 7 RESULTS OF THE CALCULATED EXTRA PRESSURES FOR DOUBLE-UNDERCUT ANGLE (50 AND 40 DEGREES) IN TWO OPPOSITE ANGLE PLACEMENT CASES.

It is evident that the calculated extra pressures for the double-undercut design are overwhelming to that for the single-undercut, taking comparison between the single-50-degree and double-50 and 40-degree at scale B=1200μm. The averaging extra pressures of

the 50-40 degree undercut group for both case 1 and case 2 are 8,829,517 Pa and 324,927

Pa, respectively. Moreover, the obtained results for Case 1 are generally more significant

than that for Case 2. Geometry wise, the configuration of Case 1 is more applicable and

practical for the infiltration process as the second inflection point in Case 1 would be able

to physically "block" the liquid surface. Example calculation is presented in the appendix.

CHAPTER 4 NUMERICAL ANALYSIS AND SIMULATIONS

Prior to the numerical analysis, there are a few factors that need to be considered. First. the analytical model was constructed based on the 2-Demensional Cartesian system, and the calculation of extra pressure for the designed double-undercut structure was based on the simple addition hypothesis. In addition, the behavior of the wetting process, the liquid-air interface of the water droplet to be specific, plays an important role in the account for extra pressure that the system can withstand. Furthermore, to ensure the improvement of the double-undercut designs, the numerical analysis aims to estimate and quantify hydrophobicity's stability via various simulations. The simulation is tailored to a particular substrate material with specified geometries with re-entrant angles and configurations. Therefore, the simulation of the double-undercut designs was conducted in COMSOL Multiphysics, as it has all the features mentioned above and offers visualized volume fractions of the fluid-solid-air system. The process of fluid infiltration and the fluid-air interface evolution as functions of the applied pressure were captured using a Horizontal-set approach in Laminar Two-Phase Flow. Yan et al. [48] have conducted similar simulations on mechanically modified micro-array porous structures to determine the critical intrinsic contact angles, which showed a linear relationship with the external pressures. Thus, the critical pressure for Cassie-Baxter to Wenzel transition can be obtained by reversing the intrinsic contact angle method for the specific substrate material. So, COMSOL Multiphysics was adopted for the numerical simulation of each design discussed in this paper.

The apparent contact angle generally describes the behavior of liquid-gas and liquid-solid interfaces dependent on the inherent contact angle. With horizontal-set

function φ, representing the volume fraction of the liquid phase in a meta-stable state, the evolution liquid-gas interface is described by:

$$\frac{\partial \varphi}{\partial t} + u \cdot \nabla \varphi = \gamma \nabla \cdot \left[\varepsilon \nabla \varphi - \varphi(1 - \varphi) \frac{\nabla \varphi}{|\nabla \varphi|} \right] \qquad \text{Eq. 41}$$

where φ=1 at the liquid phase and φ=0 at the gas phase. Meanwhile, the thickness of the defined transition surface is ε; the maximum flow velocity of the liquid, namely the reinitialization parameter, is γ; and the fluid velocity is u. The dimensions for the geometry setup have been discussed in the analytical section. However, only half of the system
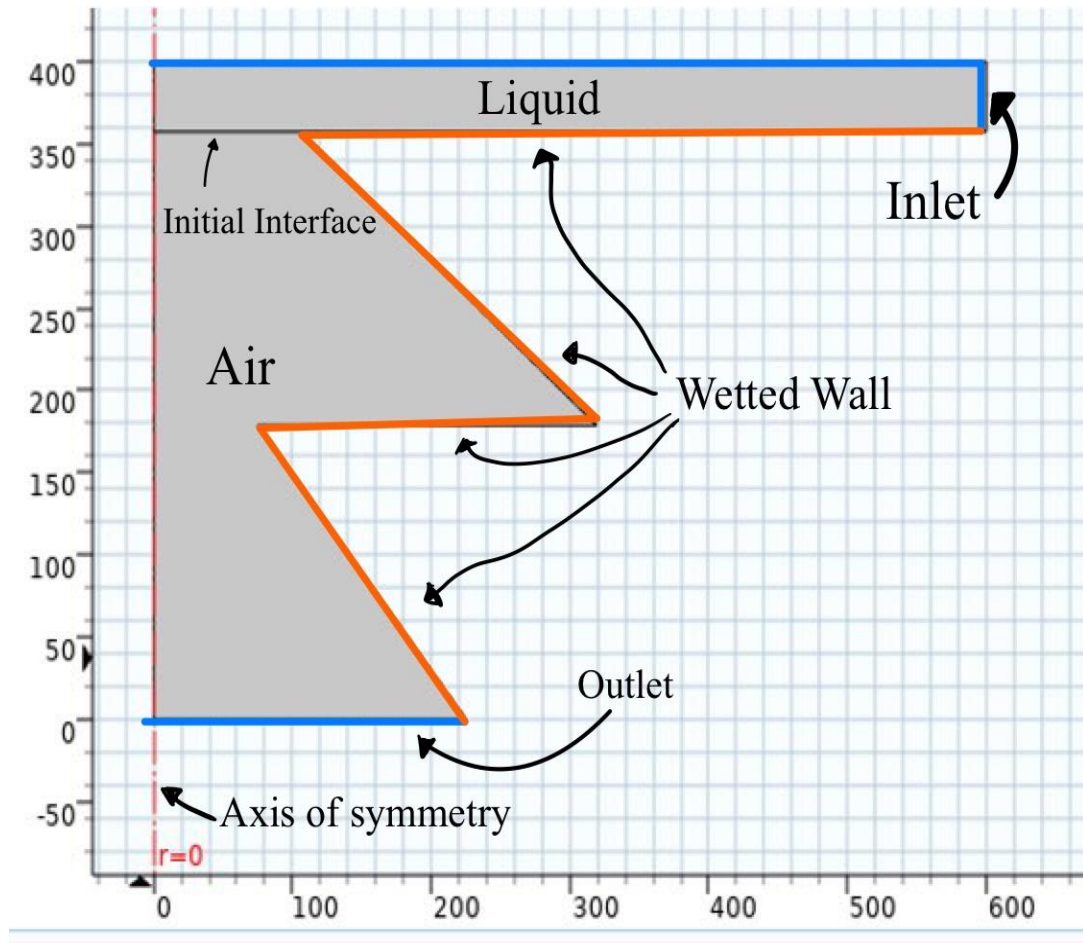

FIGURE 21. SCREENSHOT OF GEOMETRY SETUP (DOUBLE-UNDERCUT: 50 AND 40 DEREES) IN COMSOL MULTIPHYSICS FOR SIMULATION

43

shown in Figure 21 has been modeled due to the symmetry. In addition, this mirrored configuration setup would consequently be timesaving during simulation but still represents and reflects the behaviour of a 3-Dimensional (surface) wetting.

Several parameters that remained constant throughout the simulation needed to be defined to proceed with the simulation. Boundary conditions, such as inlet, outlet, and wetted wall, are assigned as it is shown in Figure 21. The volume fraction for whole wetting condition (liquid) is set to be 1, the initial state before water droplet enters thru the inlet is 0. The external pressure is applied to "liquid" zone (Figure 21). The initial interface represents the liquid-gas interface which propagates along the wetted wall according to applied external pressure at the inlet. Materials were set as liquid-water and gas-air. Surface tension is set to be 0.072 N/m(water), while a smooth silicon substrate's inherent water contact angle is 53.5°. Also, gravity is accounted for in the simulation. The desired thickness of the liquid-gas transition surface ε is 5×10^{-7} m. With a smaller thickness value, no noticeable difference will appear on both right-angle and obtuse-angle inflection points [18]. The denser mesh was configured at end of the edges of the structures and inflection points，as the infiltration behavior gets complex around them due to the fluctuation of the liquid-air interface before residing at the equilibrium points.

Table 8 shows the obtained results from the simulations of three different permutations of undercut angles with Case 1 configuration. The average extra pressure of the double-undercut design is 840 Pa. The height for each double-undercut group is identical to that of the larger single-undercut angle. The volume fraction of the fluid graph is presented in Figure 22, which illustrates the liquid-gas interfacial movement throughout the infiltration process.

Extra Pressure Double-undercut		
Undercut Angle (Degree)	Extra Pressure (Pascal)	Height (μm)
50, 36 deg	810±10	357.5260778
50, 40 deg	860±10	357.5260778
40, 36 deg	840±10	251.7298894

Table 8 EXTRA PRESSURE FOR DOUBLE-UNDERCUT CONFIGURATIONS WITH THREE DIFFERENT PERMUTATIONS OF UNDERCUT ANGLES (50, 36; 50, 40; 40, 36)
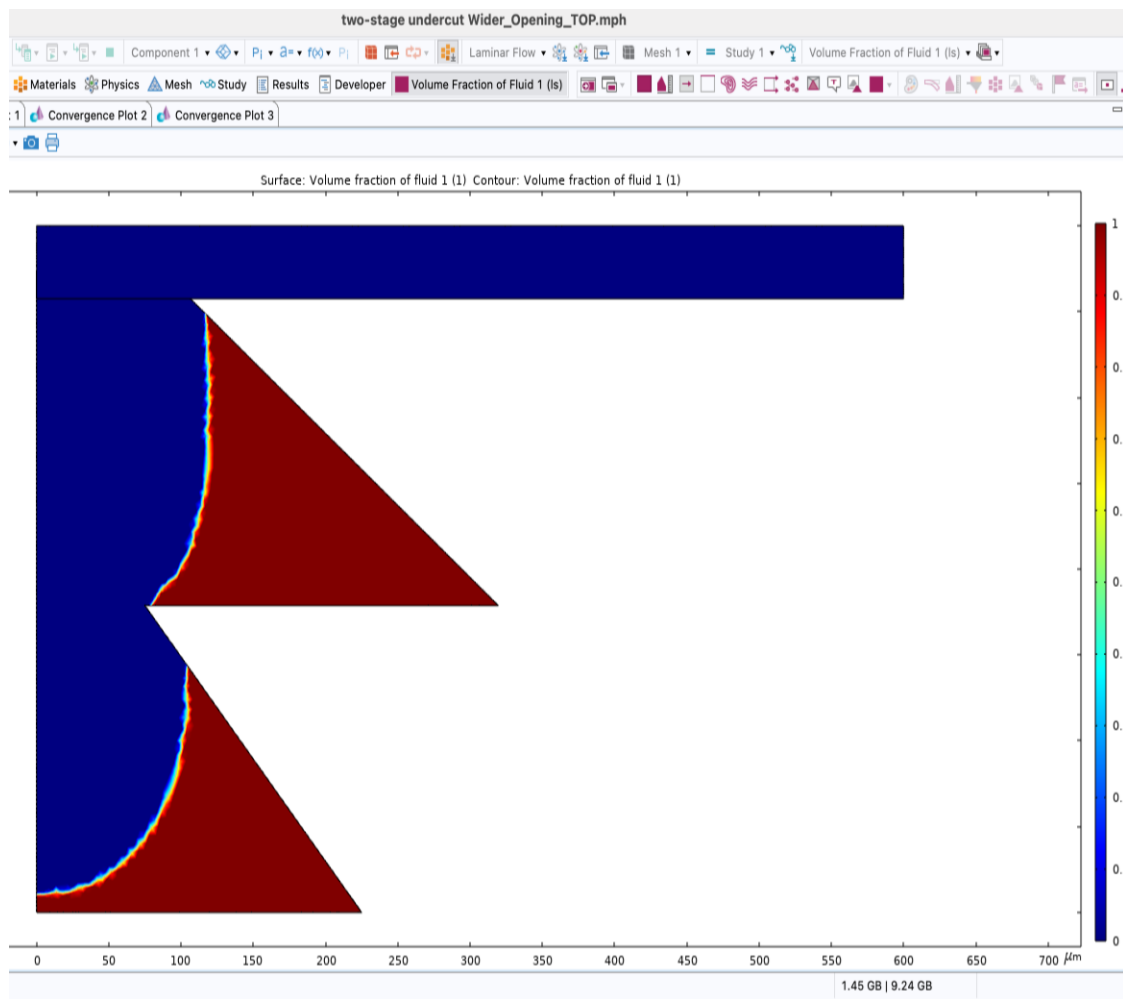
FIGURE 22. SCREENSHOT OF THE EXTRA PRESSURE SIMULATION ON THE 50° AND 40° DOUBLE-UNDERCUT ANGLES DESIGN

As the pressurized fluid (colored in blue in Fig 22) came through the system's inlet, the liquid-air interface started propagating downward, passing the first inflection point and experiencing the first "Canthotaxis" and then "Laplace breakthrough" wetting transitions as illustrated in Figures 23 and 24. These two conditions were introduced, mainly for the triangular, inward-sloped, "undercut" designs. The liquid-air interface exhibits similar wetting behavior at both stages, and the measurement of the extra pressure was obtained at the proximity to the bulk substrate (solid surface). For a few simulation attempts, the observed infiltration behavior is primarily a breakthrough.
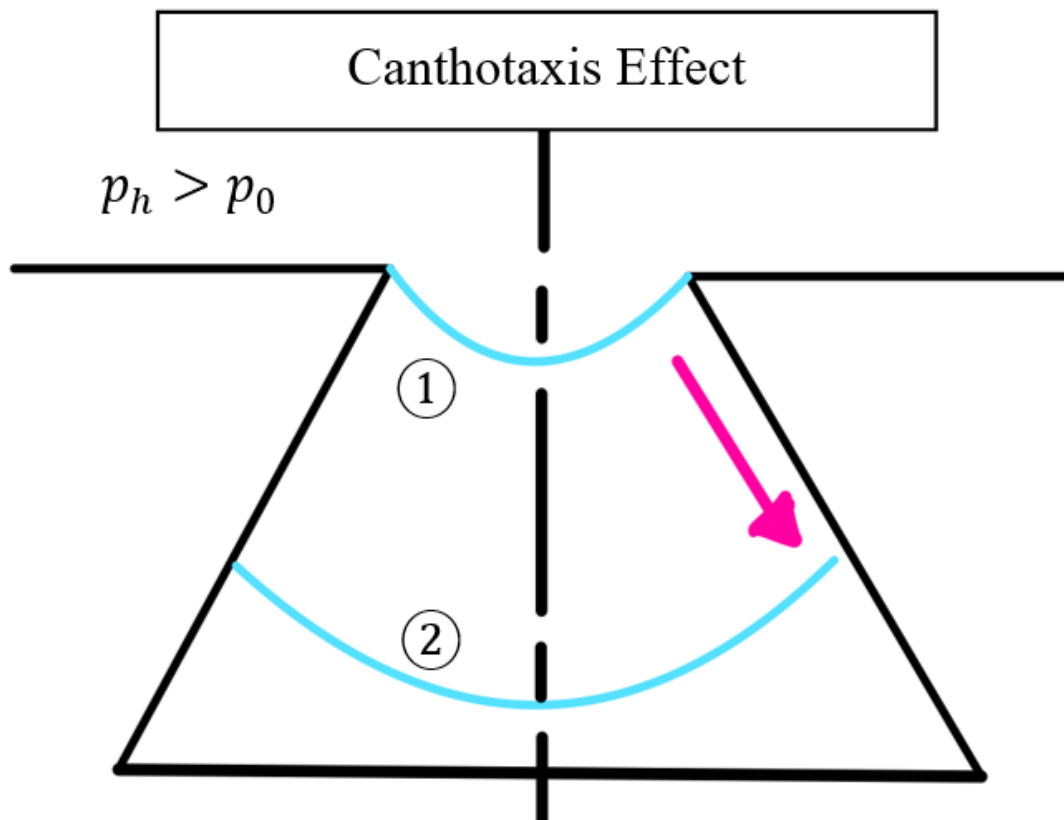
FIGURE 23. SCHEMATICS OF CANTHOTAXIS EFFECT

The driving force of the moving liquid-air interface is the predefines external
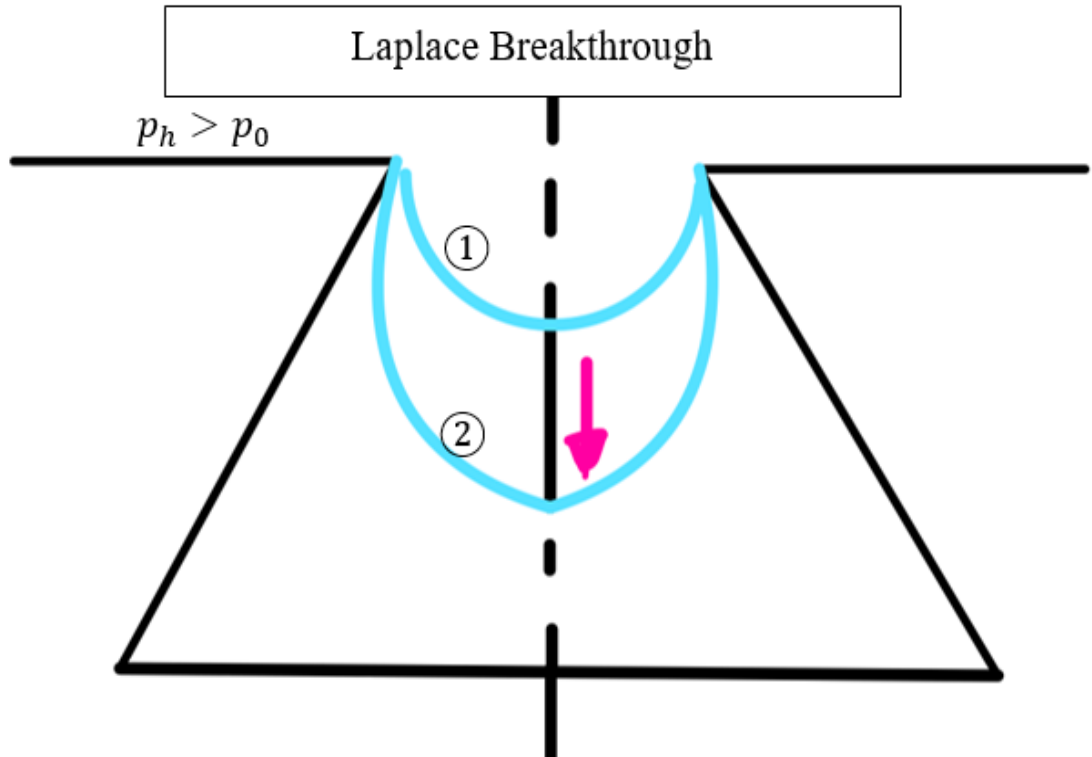
FIGURE 24. SCHEMATICS OF LAPLACE BREAKTHROUGH

which was gradually increased to reach the desired distance between the liquid-air interface

and the bottom of the "valley."

On the other hand, Case 2, shown in Figure 25, is abandoned because the inflection

point at stage 2 cannot create a stable solid-liquid-air interface due to the lack of local

potential energy minimum.
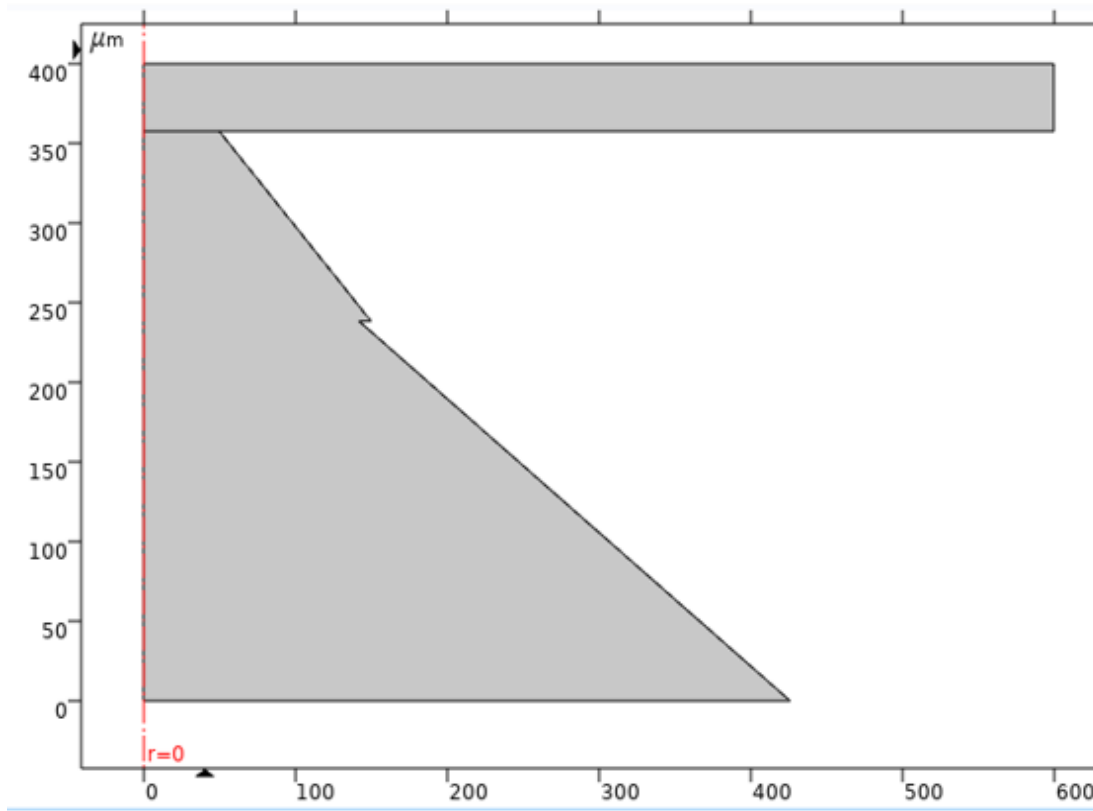
FIGURE 25. SCREENSHOT OF THE GEOMETRY FOR CASE 2, THE WIDER BOTTOM OPENING DOUBLE-UNDERCUT DESIGN (40 AND 50 DEGREES).

The extra pressure simulation results for the single-undercut configuration, as displayed in Table 9, are merely half the values of the double-undercut. At the same time, their overall heights and structure distancing were set to be the same as that of the double-undercut.

| Extra Pressure Single-undercut		
Undercut Angle (Degree)	Extra Pressure (Pascal)	Height (μm)
50	440±10	357.5260778
40	580±10	251.7298894
36	546±10	217.9627584

Table 9 EXTRA PRESSURE FOR SINGLE-UNDERCUT CONFIGURATIONS WITH UNDERCUT ANGLES OF 50, 40 AND 36 DEGREES.

In-depth simulations were also conducted to thoroughly investigate the configuration of the double-undercut design from two aspects. The first hypothesis is whether the obtained results of extra pressure for the double-undercut obey a simple addition rule of two separate single-undercut configurations. Another hypothesis is that a double-undercut design necessarily requires two different undercut angles. Tables 10 demonstrate that the simple addition rule does not apply to the double-undercut design. Considering multiple configurations of the double-undercut with the same undercut angle of 40 degrees, Table 11 demonstrates four separate sizes of the double-undercut design

Extra pressure of each Individual stage (Check if simple addition)		
Undercut Angle (Degree)	Extra Pressure (Pascal)	Height (μm)
50	722±10	178.7630389
40	819±10	178.7630389

Table 11 EXTRA PRESSURE OF THE ADDITION OF TWO SEPARATE SINGLE-UNDERCUT CONFIGURATION (40 AND 50 DEGREES).

Extra Pressure of Double-undercut for same angle			
Undercut Angle (Degree)	Extra Pressure (Pascal)	Scales & Configurations	Height (μm)
40	595±10	Full40deg + 80%	251.72+201.376
	495±10	80% + Full40deg	201.376+251.72
	235±10	180% x Full40deg	453.096
	565±10	(50%+50%) 40deg	251.730

Table 10 EXTRA PRESSURE FOR DOUBLE-UNDERCUT CONFIGURATIONS WITH SAME UNDERCUT ANGLE OF 40 DEGREE.

with the same undercut angle. None performs as the two different undercut angles. Thus, these two hypotheses are validated to be incorrect.

4.1Result and Discussion

The results obtained in the simulations demonstrate the effectiveness of the double-undercut design proposed in this study. It is essential to evaluate how the double-undercut design achieves the increase in the extra pressure. That leads to the previous discussion on the Gibbs free energy related to the infiltration process. The following Figure 26 and Figure 27 describe the relationship between the Gibbs free energy and infiltration position.

As shown, the green triangles along the curvilinear graphs represent the energy barriers where extra pressure is required for the system to reach a stable state. The red triangles indicate the system's energy local minima or equilibrium points where the liquid-air interface is stable. The depth of the potential well (the difference between the local minimum and maximum) determines the extra pressure for a double-undercut design. The liquid-air interface resides at the first equilibrium point, which is the first red triangle, due to gravitational force. Extra pressure is required to propagate the liquid-air interface along the undercut wall and overcome the surface tension. During the propagation/infiltration, air under the liquid-air interface is compressed; a portion of the work performed was converted to heat, which is non-conservative. In addition, the work for countering the no-slip(friction) condition at the liquid-solid interface moving along the wetting wall is also irreversible. Plus, the recovery of surface energy takes place when the liquid-air interface touches the second plateau of the undercut, which results in the interface leveling off at the second equilibrium point. Considering the surface energy recovery and energy losses to the non-conservative forces, the choice of undercut angles for the second stage is significantly
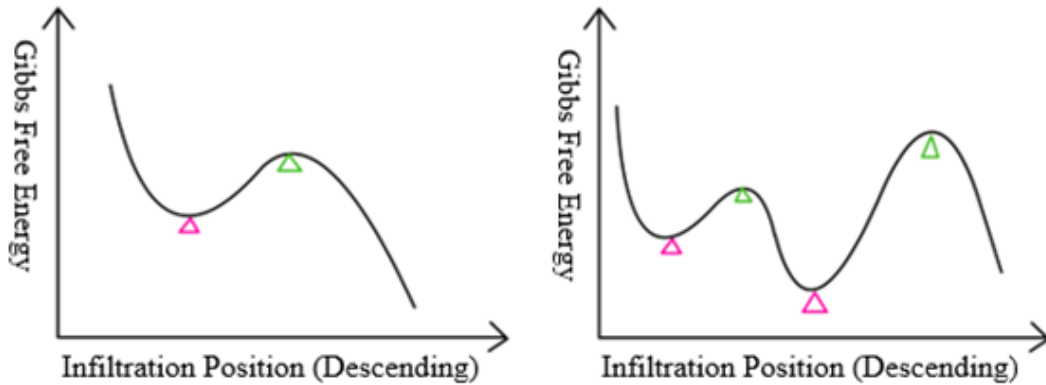
FIGURE 26. SCHEMATICS OF THE RELATIONSHIP BETWEEN GIBBS FREE ENERGY AND INFILTRATION TIME FOR BOTH SINGLE (A) AND DOUBLE (B) UNDERCUT-ANGLE DESIGN.

critical because of the distancing along the slope. For a system with the second undercut angle smaller than the first one, the second energy barrier will be lower than the first one, as indicated in Figure 27 (A). This causes the liquid-air interface to exhibit homogeneous wetting without extra pressure – a natural "phylic" (Wenzel) state. Geometry-wise, it was demonstrated in Figure 25 that the second inflection point on the second plateau is not
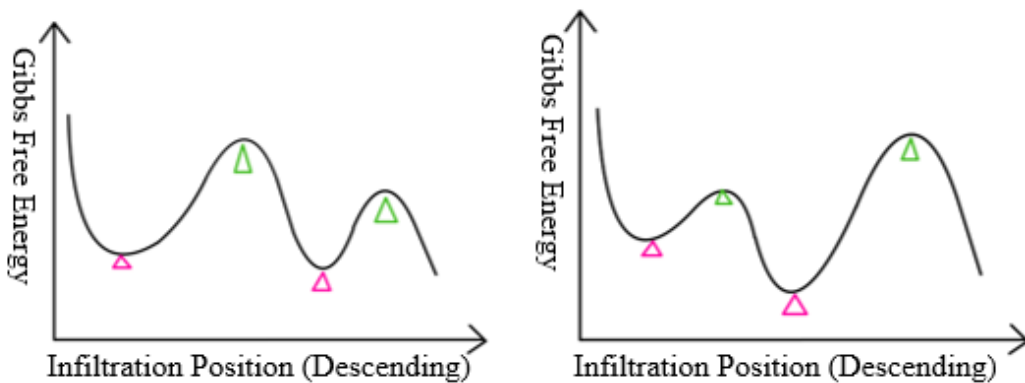

FIGURE 27. SCHEMATICS OF THE RELATIONSHIP BETWEEN GIBBS FREE ENERGY AND INFILTRATION TIME FOR BOTH DOUBLE-DISTINCT-ANGLE(A) AND DOUBLE-SAME-ANGEL (B) UNDERCUTANGLE DESIGN.

prominent as opposed to the wetted wall. However, with the observed wetting behavior and validated hypothesis of what the composition of the extra pressure would be regarding the proposed double-undercut designs, the inverse sequence of undercut angles, simply a smaller angle at the second stage offers a wider propagation distance for the liquid air interface, which leads to a higher energy barrier for the system, meaning larger extra pressure is needed to reach the homogeneous wetting state. Moreover, the configuration of the same undercut angles for both stages did not provide a significant benefit in withstanding larger extra pressure, according to the comparison between Table 4-4 and Table 4-2. The same reasoning explains why the second energy barrier may not accommodate the surface energy recovery and the non-conservative work, and even failing to sustein larger extra pressure than the single undercut design.

Therefore, it is evident that the double-undercut system, as proposed, is considerably more stable than the single-undercut system in terms of undertaking extra pressures. Furthermore, the visualization of the double-undercut design is demonstrated in Figures 28 & 29. The geometry and distancing are identical to the 1200 μm-scale in Table 3, and the patterns are aligned in arrays for uniformity. An overlooking view of the patterned sample is also provided in Figure 29. Even though the main focus of this study is the ability to withstand external hydrostatic pressures, these four different shapes of structure would be utilized for future experiments, such as sliding tests, pin-on-disk tests, etc. Thus, four distinct shapes were distributed at each corner of the rectangular specimen.
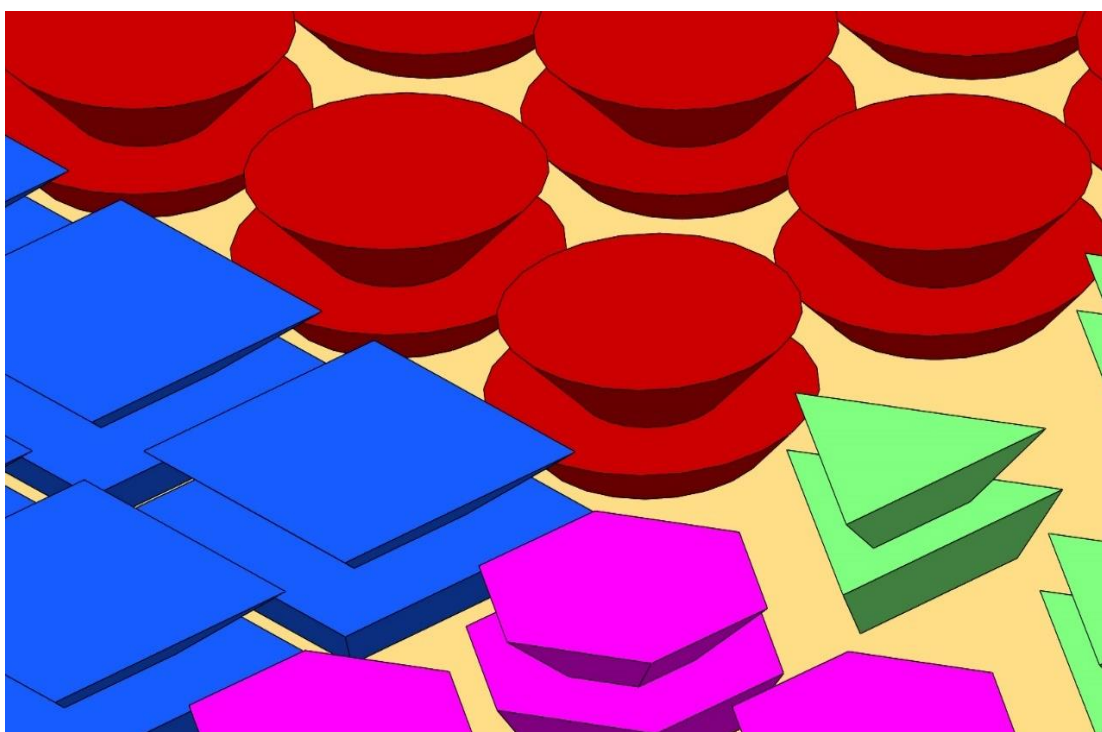
FIGURE 28. 3D DRAWING OF CIRCULAR, TRIANGULAR, RECTANGULAR, AND HEXAGONAL SHAPES OF DOUBLE-UNDERCUT STRUCTURES.
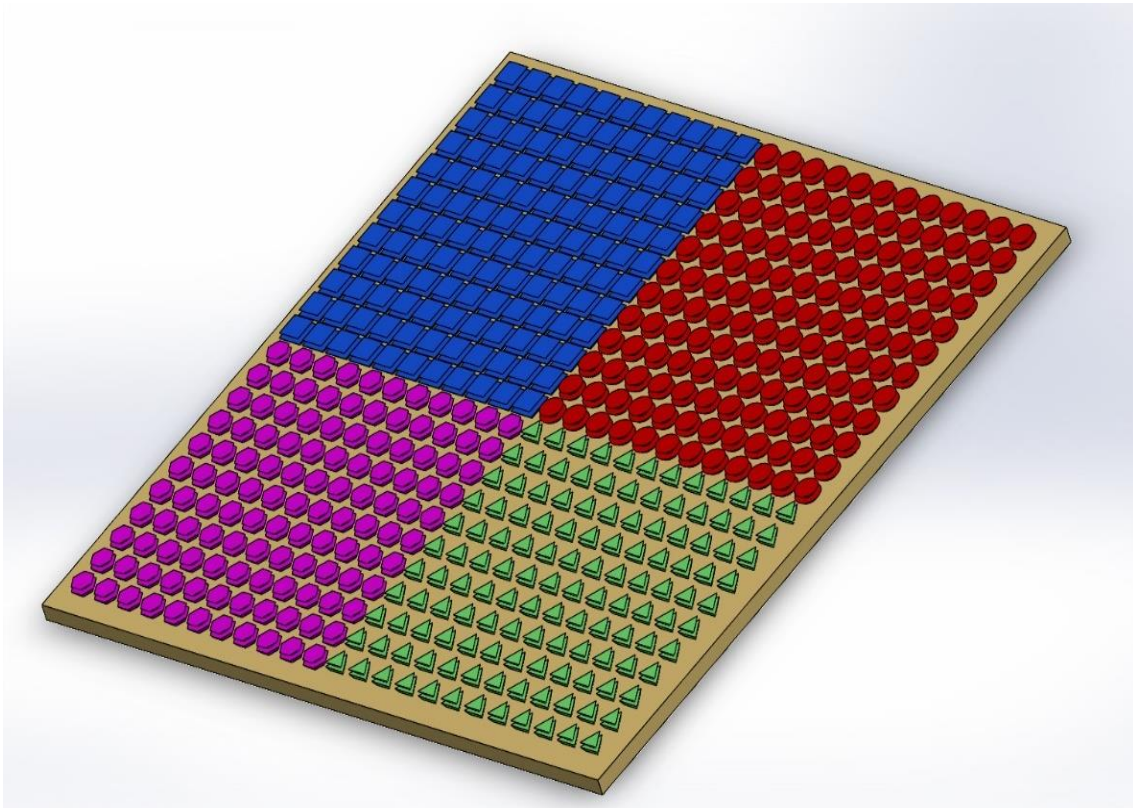
FIGURE 29. THE OVERLOOKING VIEW OF THE 3D DRAWING FOR THE DOUBLE-UNDERCUT SYSTEM IN CIRCULAR, TRIANGULAR, RECTANGULAR, AND HEXAGONAL SHAPES.

CHAPTER 5 EXPERIMENTAL SETUP AND PROCEDURES

It is essential to select the appropriate specimens before initiating experiments. Various mechanical and chemical methods exist to achieve the topography change for the desired substrate. However, the consideration of homogeneity of arrays of patterns is primary. The specimen also is required to satisfy the proof-of-concept and be approachable for fabrication. From what has been mentioned in previous chapters, PolyMUMPs fabrication system was adopted for experiment preparation.

As discussed, the polysilicon layers in the PolyMUMPs systems have specific thicknesses. The gap between two neighboring units is filled with oxides, also known as the sacrificial layer. The removal of such layer utilizes certain etching methods and generates a step-like structure with three polysilicon layers stacking up on each other, indicated in Figure 30, which is a 3D drawing of the cross-sectional view. Namely, the layers from bottom to top are the substrate (silicon wafer), Poly 0, Poly 1, and Poly 2. The applicable undercut angle/slope within the PolyMUMPs system is pointed out as angle α by the red arrow in Figure 30. Moreover, two corresponding inflection points (1 and 2) represent two energy barriers, which are also within the infiltration process.
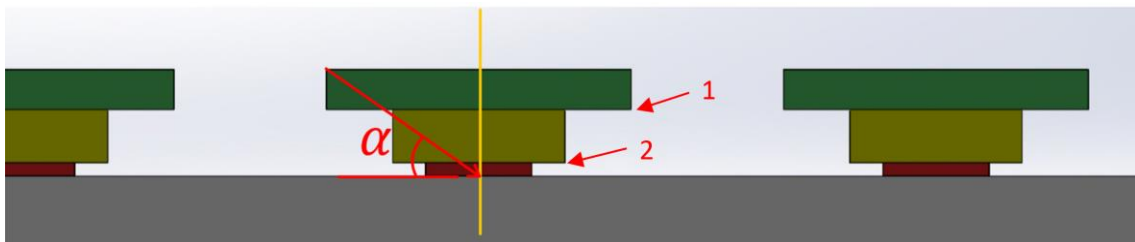

FIGURE 30. THE CROSS-SECTIONAL VIEW OF POLYSILICON LAYERS IN THE POLYMUMPS SYSTEM.

5.1 Geometry configuration in L-edit

The initial sizing discussed in Chapters 2 and 3 is not applicable in the PolyMUMPs system due to the restraints in fabrication, including the inability to create undercut slopes and the predefined sequence and thickness for each layer. The specified thicknesses for each polysilicon layer and the sacrificial layers (oxides, Anchor1 and Poly1-Poly2 Via) are listed in Table 12, and the corresponding stacking sequence from the bottom-up is from Poly 0 to Poly 2.

	Thickness(µm)
Poly 0	0.50
Anchor 1	2.00
Poly 1	2.00
Poly1-Poly2 Via	0.75
Poly 2	1.50

Table 12 THICKNESSES FOR THE ESSENTIAL LAYERS IN THE POLYMUMPS SYSTEM**.**

The silicon wafer is a 4.75µm by 4.75µm squared chip, and the determinant sizing factor became the overall height of the Poly-silicon layers, while the sacrificial layers will be etched away for the final product. There are four different undercut angles (20, 35, 30, and 35 degrees) have been chosen for the fabrication, and all of them should be less than the inherent contact angle. The added height of three polysilicon layers is 4µm, the greatest width, Poly 2, of the structure can be determined using trigonometry. The widths of the rest two layers, Poly 1 and Poly 0 are two-thirds, and one-third of the Poly 2 layer, respectively. For the same increment in width, it guarantees the two inflection points

prominent enough along the infiltration path, where the energy barrier are capable of withstanding more Gibbs free energy. The obtained value in width from the undercut angle is the b_3, and widths for Poly 1 and Poly 0 are indicated as b_2 and b_1, which have been labeled in Figure 23, respectively. An example of the dimension for the squared-shape PolyMUMPs undercut design is given in Table 13. To achieve a higher undercut angle, the widths for the polysilicon layers became shorter owing to the fixed structure height. Correspondingly, the center-to-center distance (B) of two neighboring units is also getting smaller with increasing undercut angles. Thus, the undercut angles that qualify the
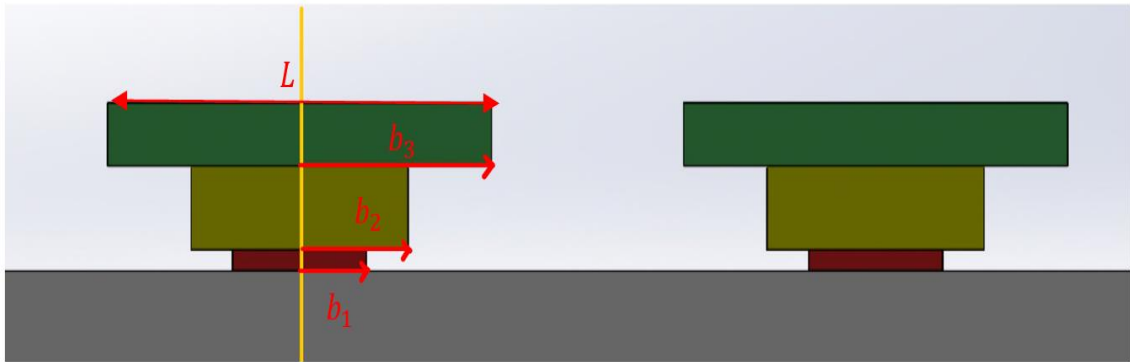
FIGURE 31. LABELS FOR EACH POLY-SILICON LAYER IN THE POLYMUMPS SYSTEM.

Undercut angle	b1(μm)	b2(μm)	b3(μm)	L(μm)	B(μm)
20	3.25	7.5	11	22	33
25	3	5.75	8.75	17.5	25.75
30	2.75	5.5	7	14	21
35	2	5.25	5.75	11.5	17.25

Table 13 THE DIMENSION OF A SQUARED-SHAPE UNDERCUT DESIGN IN THE POLYMUMPS SYSTEM.

hydrophobic criteria and are able to be fabricated are restricted to a maximum of 35 degrees.

5.2 Details in design editing

It is essential to master all the techniques provided in the design software (L-edit) to achieve the most desirable output and precision for fabrication. The snap cell function was turned off for better accuracy due to the limitation of the minimal grid size (1µm) since the resolution of the dimensions is to the hundredth of µm. Each Polysilicon layer, including the sacrificial layers, was specified with unique GDSII (Graphic Data System – Version II) numbers, which store the layers' information and the 2D geometry of the design ("Tanner EDA L-edit," Robert White, 2012). The following figures (Fig. 32-36) are the steps for adding up each essential layer for the hexagonal-shaped undercut structure in L-edit, and the related GDSII number is indicated in the "Layer Palette"".

FIGURE 32. 2D DRAWING OF THE POLY-SILICON LAYER: POLY 0 WITH GDSII NUMBER 13 IN L-EDIT.

FIGURE 33 2D DRAWING OF THE SACRIFICIAL LAYER: ANCHOR 1 WITH GDSII NUMBER 43 IN L-EDIT.
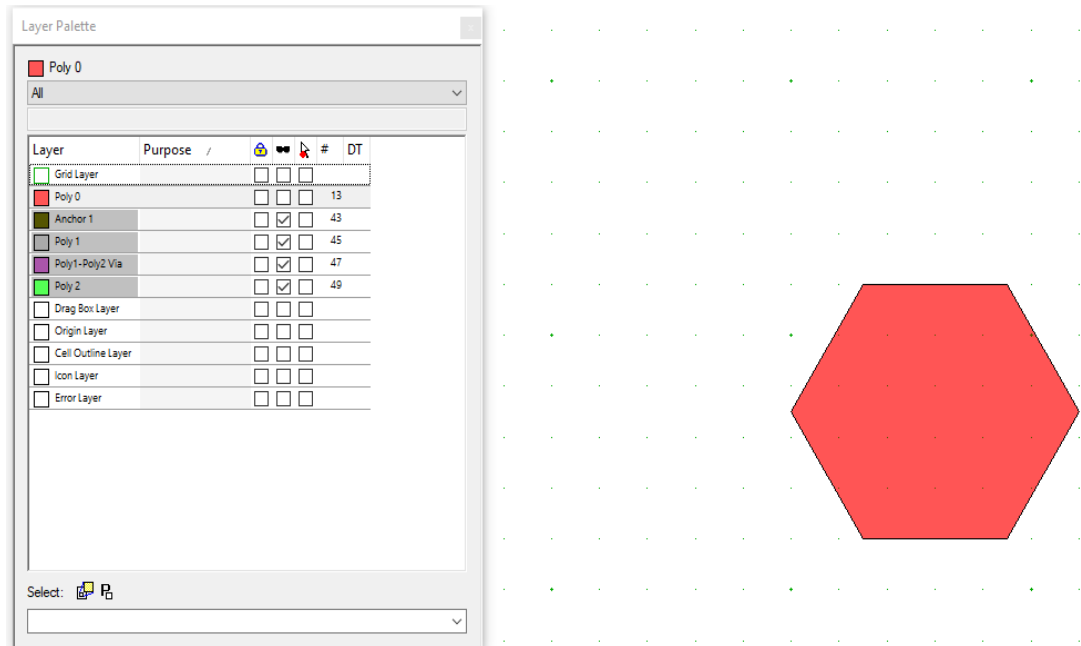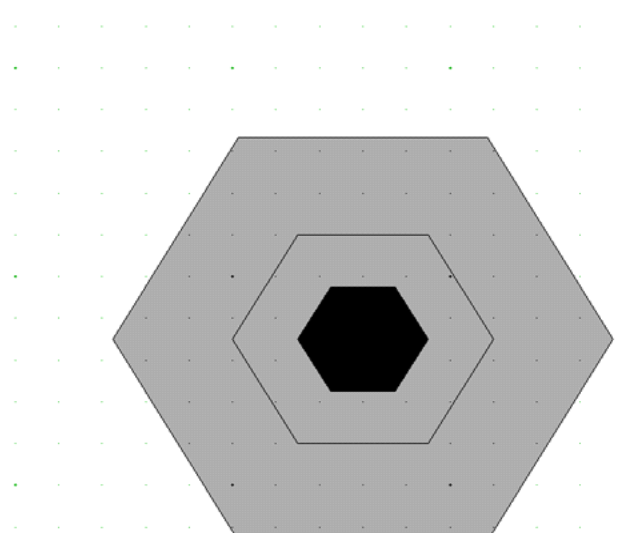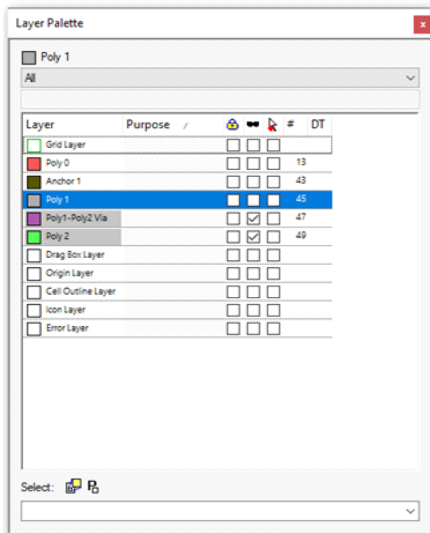

FIGURE 34. 2D DRAWING OF THE POLY-SILICON LAYER: POLY 1 WITH GDSII NUMBER 45 IN L-EDIT.
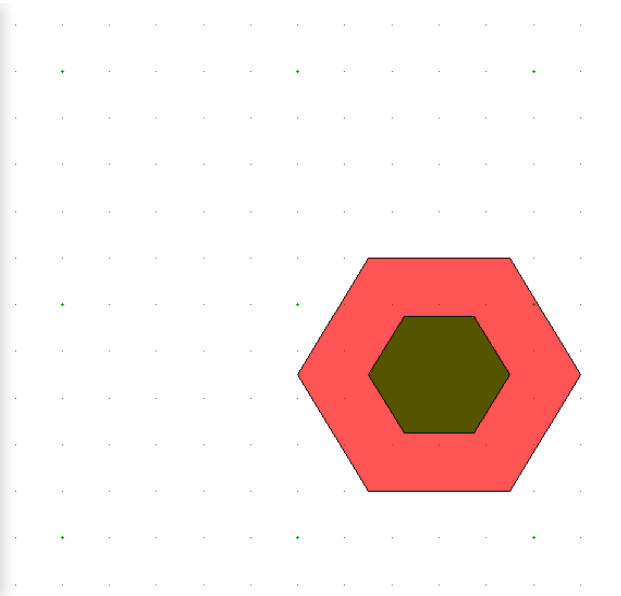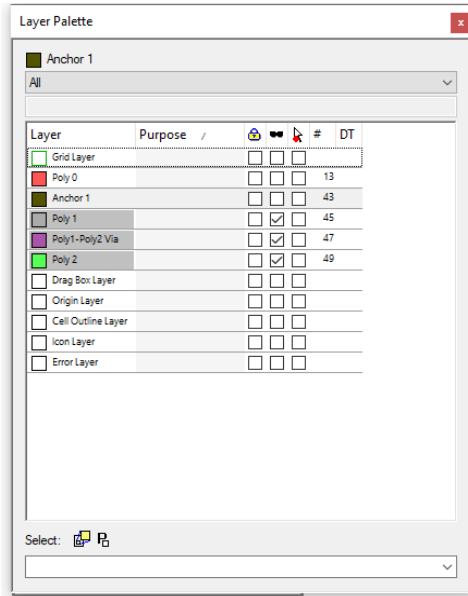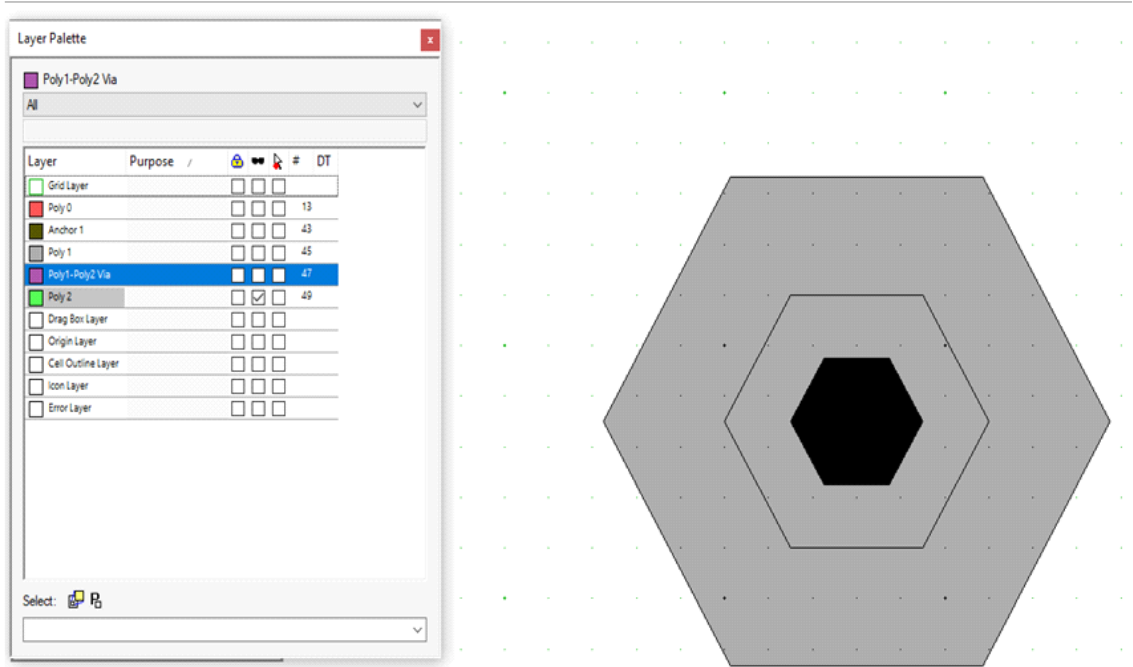
FIGURE 35. 2D DRAWING OF THE SACRIFICIAL LAYER: ANCHOR 1 WITH GDSII NUMBER 47 IN L-EDIT.
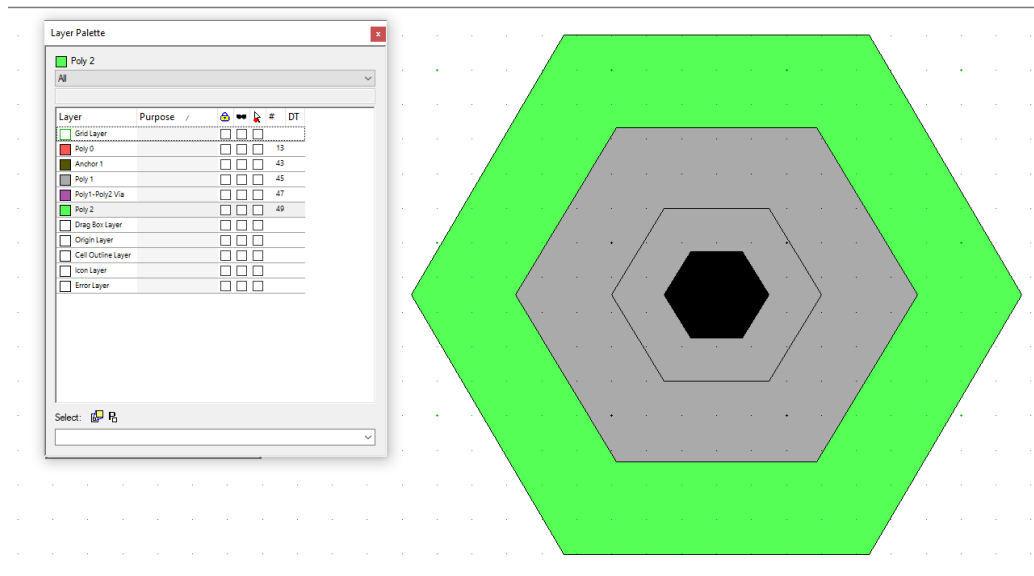
FIGURE 36. 2D DRAWING OF THE POLY-SILICON LAYER: POLY 1 WITH GDSII NUMBER 45 IN L-EDIT.
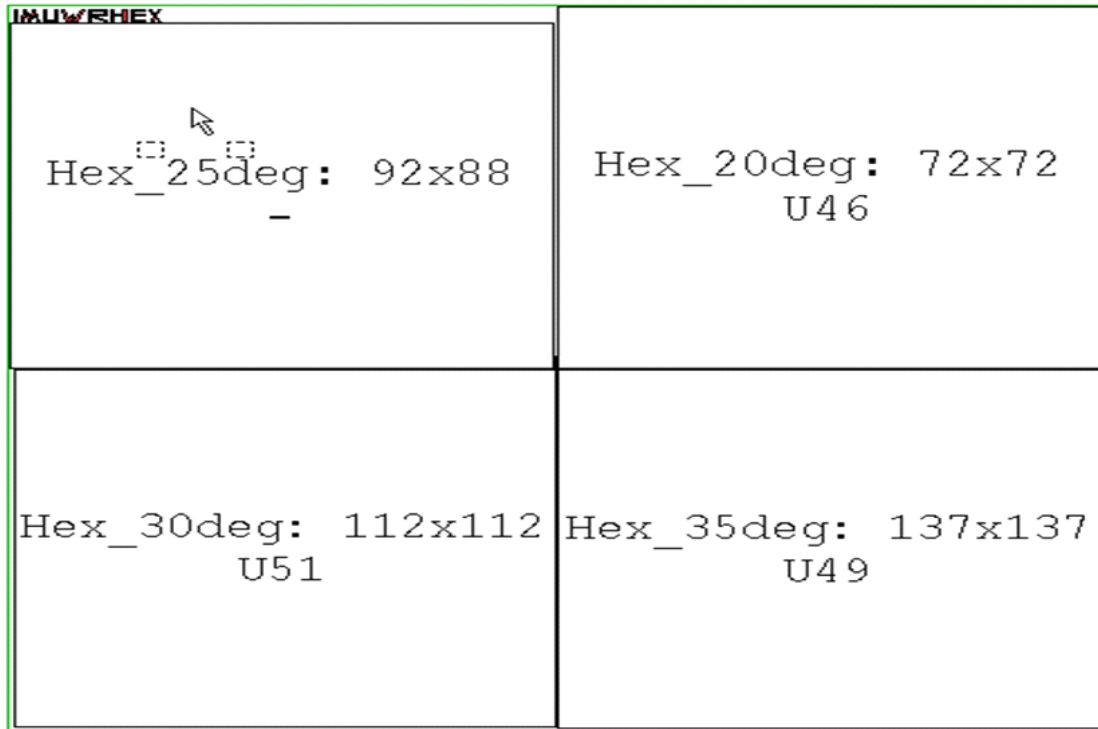
FIGURE 37. THE ARRAY DISTRIBUTION OF UNDERCUT ANGLES (20, 25, 30, AND 35 DEGREES) WITH THE CORRESPONDING GROUP SIZES (COLUMN × ROW). OUTLINES IN GREEN ARE THE BOUNDARY FOR THE SILICON WAFER.

The same approach was used in other shapes of the structure. With a single unit being constructed, the cell arraying technique is required for arranging a group of identical units. The size of the silicon wafer restrains the number of rows and columns for the array of units. To accommodate four different undercut angles for a specific shape of the structure, array groups are evenly distributed among the silicon wafer demonstrated in Figure 37. A total of four silicon wafers were designed for fabrication.

CHAPTER 6 CONCLUSION

To summarize the outcomes of this study, there are three main achievements analytical, numerical, and experimental (to be completed). Both analytical and numerical approaches have gained agreement in that the hierarchical structure with undercut slopes surface patterning assures excellent capability of withstanding more extra pressure.

The analytical method has generally described the potential of doubling the extra pressure by comparing the double to single undercut structure. The calculated extra pressure ascends drastically with an infinitely small denominator. Plus, the extra pressure for the double-undercut design was determined as a simple addition of the extra pressure values from each stage. Hence, a numerical analysis has been conducted to verify the predicted wetting behavior. Within the simulation software COMSOL Multiphysics, which features the traceable volume fraction of fluid, a systematic study shows a significant gain in extra pressure for the double-undercut design, averaging around 1000 Pascals. The proposed design was verified to be effective only under the specific sequence and combination of two distinct undercut angles. The hypotheses of simple addition and double-undercut with the same angles were proven faulty.

Regarding the infiltration process, both Laplace Breakthrough and Canthotaxis effects were observed. Future experiments will cover the apparent contact angle on the patterned polysilicon wafer. Moreover, the specimen will be placed under pressure in a pressurized chamber for it to experience a transition from the heterogeneous, Cassi-Baxter wetting regime to the homogeneous Wenzel state wetting regime. The SEM of such a sample will show the severeness of the deformation phenomenon or the presence of a potential

"necking" phenomenon. Furthermore, the obtained results from the abovementioned experiments would verify the analytical and numerical predictions. Thus, they will generally be able to predict and conclude the infiltration behaviors and estimate extra pressure gain for the hierarchical structure with undercut slopes regarding the protrusion type of mechanical surface patterning technique.

REFERENCES

[1]   W. Barthlott and C. Neinhuis, "Purity of the sacred lotus, or escape from contamination in biological surfaces," *Planta*, vol. 202, no. 1, 1997, doi: 10.1007/s004250050096.

[2]   X. Gao and L. Jiang, "Water-repellent legs of water striders," *Nature*, vol. 432, no. 7013, 2004, doi: 10.1038/432036a.

[3]   D. W. Bechert, M. Bruse, W. Hage, and R. Meyer, "Fluid mechanics of biological surfaces and their technological application," *Naturwissenschaften*, vol. 87, no. 4, pp. 157–171, 2000.

[4]   R. N. Wenzel, "Resistance of solid surfaces to wetting by water," *Ind Eng Chem*, vol. 28, no. 8, 1936, doi: 10.1021/ie50320a024.

[5]   A. B. D. Cassie and S. Baxter, "Wettability of porous surfaces," *Transactions of the Faraday Society*, vol. 40, 1944, doi: 10.1039/tf9444000546.

[6]   A. Marmur, "Solid-surface characterization by wetting," *Annual Review of Materials Research*, vol. 39. 2009. doi: 10.1146/annurev.matsci.38.060407.132425.

[7]   Y. C. Jung and B. Bhushan, "Contact angle, adhesion and friction properties of micro-and nanopatterned polymers for superhydrophobicity," *Nanotechnology*, vol. 17, no. 19, 2006, doi: 10.1088/0957-4484/17/19/033.

[8]   A. Tuteja *et al.*, "Designing superoleophobic surfaces," *Science (1979)*, vol. 318, no. 5856, 2007, doi: 10.1126/science.1148326.

[9]   S. Lyu, D. C. Nguyen, D. Kim, W. Hwang, and B. Yoon, "Experimental drag reduction study of super-hydrophobic surface with dual-scale structures," *Appl Surf Sci*, vol. 286, pp. 206–211, 2013.

[10]   M. Miwa, A. Nakajima, A. Fujishima, K. Hashimoto, and T. Watanabe, "Effects of the surface roughness on sliding angles of water droplets on superhydrophobic surfaces," *Langmuir*, vol. 16, no. 13, pp. 5754–5760, 2000.

[11]   M. Ma, Y. Mao, M. Gupta, K. K. Gleason, and G. C. Rutledge, "Superhydrophobic fabrics produced by electrospinning and chemical vapor deposition," *Macromolecules*, vol. 38, no. 23, 2005, doi: 10.1021/ma0511189.

[12]   A. Singh, L. Steely, and H. R. Allcock, "Poly[bis(2,2,2-trifluoroethoxy)phosphazene] superhydrophobic nanofibers.," *Langmuir*, vol. 21, no. 25, pp. 11604–11607, Dec. 2005, doi: 10.1021/la052110v.

[13] M. Zhu, W. Zuo, H. Yu, W. Yang, and Y. Chen, "Superhydrophobic surface directly created by electrospinning based on hydrophilic material," *J Mater Sci*, vol. 41, no. 12, pp. 3793–3797, 2006, doi: 10.1007/s10853-005-5910-z.

[14] F. O. Ochanda, M. A. Samaha, H. V. Tafreshi, G. C. Tepper, and M. Gad-el-Hak, "Fabrication of superhydrophobic fiber coatings by DC-biased AC-electrospinning," *J Appl Polym Sci*, vol. 123, no. 2, pp. 1112–1119, 2012.

[15] M. A. Samaha, H. Vahedi Tafreshi, and M. Gad-el-Hak, "Modeling drag reduction and meniscus stability of superhydrophobic surfaces comprised of random roughness," *Physics of Fluids*, vol. 23, no. 1, 2011, doi: 10.1063/1.3537833.

[16] J. R. Wendt, G. A. Vawter, R. E. Smith, and M. E. Warren, "Nanofabrication of subwavelength, binary, high-efficiency diffractive optical elements in GaAs," *Journal of Vacuum Science and Technology B: Microelectronics and Nanometer Structures*, vol. 13, no. 6, 1995, doi: 10.1116/1.588248.

[17] D. C. Flanders, "Replication of 175-Å lines and spaces in polymethylmethacrylate using x-ray lithography," *Appl Phys Lett*, vol. 36, no. 1, pp. 93–96, 1980.

[18] I. I. Smolyaninov, D. L. Mazzoni, and C. C. Davis, "Near-field direct-write ultraviolet lithography and shear force microscopic studies of the lithographic process," *Appl Phys Lett*, vol. 67, no. 26, pp. 3859–3861, 1995.

[19] Y. G. Schneider, "Formation of surfaces with uniform micropatterns on precision machine and instruments parts," *Precis Eng*, vol. 6, no. 4, 1984, doi: 10.1016/0141-6359(84)90007-2.

[20] I. Etsion, "State of the art in laser surface texturing," *Journal of Tribology*, vol. 127, no. 1. 2005. doi: 10.1115/1.1828070.

[21] A. Toloei, "The effect of surface patterning and unidirectional roughness on corrosion of metals," 2014.

[22] S. J. Abbott and P. H. Gaskell, "Mass production of bio-inspired structured surfaces," *Proc Inst Mech Eng C J Mech Eng Sci*, vol. 221, no. 10, 2007, doi: 10.1243/09544062JMES540.

[23] C. M. Sotomayor Torres, *Alternative Lithography: Unleashing the Potentials of Nanotechnology*. 2003.

[24] A. Cowen, B. Hardy, R. Mahadevan, and S. Wilcenski, "PolyMUMPs design handbook," *Memscap Inc*, vol. 13, 2011.

[25] J. Ou, B. Perot, and J. P. Rothstein, "Laminar drag reduction in microchannels using ultrahydrophobic surfaces," *Physics of fluids*, vol. 16, no. 12, pp. 4635–4643, 2004.

[26] J. Ou and J. P. Rothstein, "Direct velocity measurements of the flow past drag-reducing ultrahydrophobic surfaces," *Physics of fluids*, vol. 17, no. 10, p. 103606, 2005.

[27] P. Joseph *et al.*, "Slippage of water past superhydrophobic carbon nanotube forests in microchannels," *Phys Rev Lett*, vol. 97, no. 15, p. 156104, 2006.

[28] R. Truesdell, A. Mammoli, P. Vorobieff, F. van Swol, and C. J. Brinker, "Drag reduction on a patterned superhydrophobic surface," *Phys Rev Lett*, vol. 97, no. 4, 2006, doi: 10.1103/PhysRevLett.97.044504.

[29] M. B. Martell, J. B. Perot, and J. P. Rothstein, "Direct numerical simulations of turbulent flows over superhydrophobic surfaces," *J Fluid Mech*, vol. 620, pp. 31–41, 2009.

[30] C. J. Teo and B. C. Khoo, "Analysis of Stokes flow in microchannels with superhydrophobic surfaces containing a periodic array of micro-grooves," *Microfluid Nanofluidics*, vol. 7, no. 3, pp. 353–382, 2009.

[31] R. J. Daniello and J. P. Rothstein, "Turbulent drag reduction using superhydrophobic surfaces," in *APS Division of Fluid Dynamics Meeting Abstracts*, 2008, vol. 61, p. GA-003.

[32] C. Lee, C. H. Choi, and C. J. Kim, "Structured surfaces for a giant liquid slip," *Phys Rev Lett*, vol. 101, no. 6, 2008, doi: 10.1103/PhysRevLett.101.064501.

[33] M. A. Samaha, H. V. Tafreshi, and M. Gad-El-Hak, "Influence of flow on longevity of superhydrophobic coatings," *Langmuir*, vol. 28, no. 25, 2012, doi: 10.1021/la301299e.

[34] M. S. Bobji, S. V. Kumar, A. Asthana, and R. N. Govardhan, "Underwater sustainability of the 'Cassie' state of wetting," *Langmuir*, vol. 25, no. 20, 2009, doi: 10.1021/la902679c.

[35] M. Sakai, T. Yanagisawa, A. Nakajima, Y. Kameshima, and K. Okada, "Effect of surface structure on the sustainability of an air layer on superhydrophobic coatings in a water− ethanol mixture," *Langmuir*, vol. 25, no. 1, pp. 13–16, 2009.

[36] R. Poetes, K. Holtzmann, K. Franze, and U. Steiner, "Metastable underwater superhydrophobicity," *Phys Rev Lett*, vol. 105, no. 16, 2010, doi: 10.1103/PhysRevLett.105.166104.

[37] R. B. Alvarez *et al.*, "Corrosion relationships as a function of time and surface roughness on a structural AE44 magnesium alloy," *Corros Sci*, vol. 52, no. 5, 2010, doi: 10.1016/j.corsci.2010.01.018.

[38] E. Willis, "Surface finish in relation to cylinder liners," *Wear*, vol. 109, no. 1–4, pp. 351–366, 1986.

[39] M. Wakuda, Y. Yamauchi, S. Kanzaki, and Y. Yasuda, "Effect of surface texturing on friction reduction between ceramic and steel materials under lubricated sliding contact," *Wear*, vol. 254, no. 3–4, pp. 356–363, 2003.

[40] I. Etsion, "Improving tribological performance of mechanical components by laser surface texturing," *Tribol Lett*, vol. 17, no. 4, pp. 733–737, 2004.

[41] I. Etsion and L. Burstein, "A model for mechanical seals with regular microsurface structure," *Tribology Transactions*, vol. 39, no. 3, pp. 677–683, 1996.

[42] I. Etsion, Y. Kligerman, and G. Halperin, "Analytical and experimental investigation of laser-textured mechanical seal faces," *Tribology Transactions*, vol. 42, no. 3, pp. 511–516, 1999.

[43] I. Etsion and O. Michael, "Enhancing sealing and dynamic performance with partially porous mechanical face seals," *Tribology Transactions*, vol. 37, no. 4, pp. 701–710, 1994.

[44] N. Tayebi and A. A. Polycarpou, "Reducing the effects of adhesion and friction in microelectromechanical systems (MEMSs) through surface roughening: comparison between theory and experiments," *J Appl Phys*, vol. 98, no. 7, p. 73528, 2005.

[45] N. Tayebi and A. A. Polycarpou, "Adhesion and contact modeling and experiments in microelectromechanical systems including roughness effects," *Microsystem technologies*, vol. 12, no. 9, pp. 854–869, 2006.

[46] E. Rivin, *Stiffness and damping in mechanical design*. CRC Press, 1999.

[47] V. Stoilov, "Superoleophobic Surfaces. Theoretical Feasibility," 2018.

[48] Y. Shen, G. Guo, Y. Zhang, Y. Lu, and X. Wang, "Simulation of Hydrophobicity Evaluation and Structural Optimization Design Method for Micro-Array Units," *J Surf Eng Mater Adv Technol*, vol. 8, no. 2, pp. 37–48, 2018.

VITA AUCTORIS

NAME:	Zirui Liu
PLACE OF BIRTH:	Qingdao, Shandong, China
YEAR OF BIRTH:	1996
EDUCATION:	Fort Richmond Collegiate, Winnipeg, MB, 2014
	University of Windsor, B.A.Sc., Windsor, ON, 2019
	University of Windsor, M.A.Sc., Windsor, ON, 2023